# Late Cenozoic Extension in Limni Basin
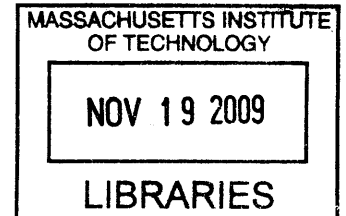
# in Northern Evia, Greece

by

Aleksandra M. Hosa

B.S. Earth, Atmospheric and Planetary Sciences
M.I.T., 2008

Submitted to the Department of Earth, Atmospheric and Planetary Sciences
in Partial Fulfillment of the Requirements for the Degree of
Master of Science in Earth and Planetary Sciences
at the Massachusetts Institute of Technology

[September]
Aug 24, 2009

Author_____

Department of Earth, Atmospheric and Planetary Sciences
Aug 24, 2009

Certified by_____

Leigh H. Royden
Thesis Supervisor

Accepted by_____

Maria Zuber
Head, Department of Earth, Atmospheric and Planetary Sciences

## Abstract

The Aegean region has undergone several episodes of extensional deformation from early Miocene to present time. Among the structures that accommodate extension are faults that bound and cut sediments within young fault-controlled sedimentary basins. The objective of this study is to add to constraints on the history of within the upper plate of the Hellenic subduction zone. In particular, this study is aimed at mapping and, eventually, dating sediments and related normal faults in the Limni-Istiea basin of northern Evia. Field mapping in the southern portion of this basin reveals eight sedimentary units and suggests several periods during which steep relief was formed within and adjacent to the basin, interspersed with periods of deposition in fluvial and shallow lacustrine environment. The three sets of faults identified in the mapped area are consistent with the orientation of structures observed at the western end of the North Aegean trough system and within the Central Hellenic shear zone. The oldest faults are low-angle, north-south trending and east-dipping; younger structures are high angle, west-east or southwest-northeast trending and generally south-dipping; the youngest faults are high-angle, northwest-southeast trending and dipping to the southwest. The paleomagnetic analyses results show clockwise rotation of the Limni-Istiea basin by 18° during or after the last stages of extension within the basin.

# Contents

## List of Figures

## List of Tables

# 1. Introduction

The tectonic evolution of Greece since 30 Ma has been dominated by the subduction of the Ionian Sea lithosphere and the associated upper plate extension. As a result, a series of Mio-Pleistocene extensional basins were created within Greece (van Hinsbergen et al., 2005). These extensional structures have accommodated a large clockwise rotation of the Aegean region (van Hinsbergen et al., 2005).

MEDUSA ('Multi-disciplinary Experiments for Dynamic Understanding of Subduction under the Aegean Sea') is a collaborative effort combining geology and geophysics and aimed at improving the understanding of the dynamics of the subducting slab lithosphere, its interaction with the surrounding mantle and its connection to surface deformation and tectonics. The Mediterranean area provides an excellent opportunity for such studies due to the fact that plate boundaries are relatively short in length, enabling the study of geophysical and geological processes at a regional scale (Figure 1-1). Also, the Hellenic system is one of just a few regional systems displaying such a rapid rate of subduction and upper plate extension. This study was undertaken as a part of the MEDUSA project and is aimed at learning more about the temporal and spatial relationships in the extension of the Hellenic upper plate by the means of field mapping and paleomagnetic analysis.

For the past decades, the Hellenic system, located between converging African and Eurasian tectonic plates, has been a subject of very active research. Among the various investigations undertaken, geodesy has provided important constraints on the relative motions of the plates. Presently, subduction beneath the portion of the system north of the Kephalonia Transform fault occurs at rates of 5-10 mm/yr. In the southern Hellenic subduction system the convergence proceeds at a higher rate of 40 mm/yr (McClusky et al., 2000) (Figure 1-2).

GPS data also show a broad zone of dextral shear and extension within the upper plate, with a rate of displacement that is approximately equal to the difference in subduction rate on the

opposite sides of the Kephalonia Transform. This zone, termed the Central Hellenic shear zone (Papanikolaou and Royden, 2007), provides structural accommodation for this difference in subduction rate. In the northeast, Central Hellenic shear zone merges into the purely strike-slip North Anatolian fault with dextral sense of movement (Figure 1-3).

The present rate of subduction and dextral shear are well constrained by the GPS data. However, the development of the varying rates of displacement along the Hellenic subduction system over time is still poorly understood. One means of constraining the temporal history of subduction along the Hellenic arc is by mapping and dating of faults within the Central Hellenic shear zone and by dating the sediments in the fault-bounded basins. This study was focused on one such basins: the Limni-Istiea basin in the northern part of Evia. The Limni-Istiea basin, filled with lower Miocene to upper Pliocene river and lacustrine deposits (Palyvos et al., 2006), appears similar to other fault-controlled basins in the region, such as the Kymi-Aliveri basin located to the south, in central Evia. This paper describes the field relations and the results of paleomagnetic analysis carried out in the southern portion of the Limni-Istiea basin.


## 2. Tectonic Setting

The Hellenic subduction system off the western coast of Greece, where the African and European plates are converging, is the major geologic feature that has created and shaped the Aegean region. In middle to late Miocene, the continuous Hellenic arc was disrupted probably due to change of the plate collision regime from continental-continental to oceanic-continental in the southern portion of the trench (Royden and Papanikolaou, 2009). Presently, subduction beneath the portion of the system north of the Kephalonia Transform fault occurs at rates of 5-10 mm/yr. In the southern Hellenic system the convergence proceeds at a higher rate of 40 mm/yr (McClusky et al., 2000). This difference in subduction rate is accommodated by the dextral

Kephalonia Transform fault in the west and by the Central Hellenic shear zone in the east. In the late Pliocene, the rate of slip along the North Anatolian fault also increased to 25 mm/yr.

Beginning in Oligocene time, the back-arc area from the Aegean to central Greece, underwent widespread extensional deformation. Extensional faults within the Central Hellenic shear zone probably began to disrupt the upper plate region beginning in middle or upper Miocene time. The initial stage of deformation within the Central Hellenic shear zone is expressed by low-angle detachment faults within the Aegean region and in mainland Greece (Papanikolaou and Royden, 2007) (Figure 2-1). During Pliocene time, the deformation style underwent a transition from low-angle northwest-southeast or southwest-northeast trending faults to high-angle nearly west-east trending structures with normal and dextral displacement (Figure 2-1). Today these faults of the Central Hellenic shear zone accommodate the difference in trench retreat rate between the northern and southern Greece and most probably also did since the time of their inception. The Pliocene-Quaternary faults of the Central Hellenic shear zone extend westwards to the Kephalonia Transform fault and eastwards to the North Anatolian fault. In the eastern part of the fault system, the Plio-Quaternary structures change their orientation to align with those of the North Anatolian fault. Structures of this age in northern Evia trend southwest-northeast.

Faults corresponding to both stages of development of the Central Hellenic shear zone are present in the vicinity of the field area. The earlier, middle-Miocene to early Pliocene stage is represented by the southwest-northeast trending and south dipping detachment to the north of Evia and another low-angle east-dipping fault on the mainland Greece parallel to the Evoikos Gulf.

# 3. Stratigraphy

In essence, field mapping in the southern part of the Limni-Istiea basin, north of the towns of Limni and Rovies revealed eight sedimentary units (Figure 3-1), forming over a 1km thick succession (Figure 3-2). The debris flows at the bottom is related to initial relief formation, which was followed by fluvial period evidenced by deposition of sandstones and mudstones. After further tilting, thick conglomerates and sandstones were deposited in a fluvial environment. A third faulting event and high relief formation was followed by shallow lake formation, in which debris flows were deposited and topped with fine lacustrine sediments.

The Limni-Istiea basin dominates the region of northern Evia. The basin contains fluvial and lacustrine deposits dated as Lower Miocene to Upper Pliocene (Palyvos et al., 2006); these are similar in age and facies to the sediments contained in other basins in central-eastern Greece, and include marls and marly limestones, sandstones and conglomerates (Mettos et al., 1992).

Field observations undertaken during this study focused mainly on units within the depositional basin and the underlying basement units were not differentiated, although several distinct basement lithologies are present. Published descriptions identify basement units that include a Permian–Triassic volcanic complex, a thick sequence of Triassic–Jurassic carbonates of the Sub-Pelagonian unit, and ophiolites of the Late Jurassic–Early Cretaceous (Palyvos et al., 2006). These Mesozoic formations were folded during Alpine orogenesis in Paleocene–Eocene time.

The sedimentary deposits in the lower part of the Limni-Istiea basin have been dated as Lower Miocene, equivalent to formations in the Kymi-Aliveri basin of central Evia (Mettos et al., 1992). From oldest to youngest, the sequence begins with pebbly conglomerates and limestones overlain by intensively tectonized grey-green pelites interbedded with clays, sands and sandstones. The thickness of these sediments (conglomerates through pelites) is ~200 m. Upwards, fluvio-lacustrine deposits of upper Miocene and Pliocene age are laterally extensive

and consist of conglomerates, silicified sandstones and silty clays that contain mammalian fossils (Mettos et al., 1992). The succession continues with marly layers grading upwards into marly limestones and traventines. The basin sequence is terminated with a thick conglomerate sequence containing marly and sandy interbeds.

Descriptions of each of the eight mapped basinal units are given below. The descriptive name of each unit is followed by an abbreviation for that unit, and this abbreviation is used on the accompanying geological map (Figure 3-1) and on the stratigraphic column (Figure 3-2). Unit descriptions begin with the highest part of the sequence and progress downward through the basin. Additionally, the specific localities mentioned in the descriptions are shown in Figure 3-3.

### 3.1. Marl (m)

Marl comprises the areally extensive upper unit, taking up most of the southern part of the field area. Its thickness is estimated at ~100m; however this is a crude estimate because the unit is strongly tectonized and repeated several times by normal faults. Marl lies conformably on the Orange Debris Flow as observed at localities r-1 and r-2 (Figure 3-4). In general, this unit is a conglomerate with a marly matrix and marl, sandstone and limestone interbeds. However, the clasts are finer than those contained within the underlying debris flow, with clasts up to cm scale. This unit is characteristically white. Thick layers of typical white marl are common (r-3 through r-11).

A prominent outcrop is found along the road near the town of Limni at locality r-1(Figure 3-5). The exposed sequence starts with a siliciclastic bed and transitions upward into a massive marl layer ~20 m thick. At the bottom of the marl layer there are several (~10) chert nodule layers. These chert nodules are characteristic of the massive marl sequence and may be encountered at other localities: r-12, and r-13. The massive marl layer is succeeded upward by grey and brown medium grained sandstones and fine grained conglomerates (Figure 3-6). The sandstones are clearly stratified and are characterized by a low degree of cementing and high

permeability and porosity. They exhibit clear cross-stratification features indicating that this succession is not overturned.

The overlying layers with this unit are not exposed and the continuity of the succession cannot be established. However, the next outcrop along the road consists of marl interbedded with pervasive thin limestone and grey and brown sandstone layers. The limestone-rich marl is interpreted to be higher in the stratigraphic column than the pure white massive marl. At other localities in the field area white cliffs of the pervasive limestone-rich marl are also present: r-14 through r-21 (Figure 3-7).

## 3.2. Orange Debris Flow (odf)

This unit is a mixture of various siliciclastic subunits, most prominent of which is a characteristic debris flow with an orange matrix (Figure 3-8). This unit also includes a thick succession of finer grained siliciclastics (Figure 3-9). Its thickness is estimated at ~100m. The conformable transitional contact with underlying marl is observed at locality r-1. The transition is sharp but occurs without major change in the dip. Within the Orange Debris Flow unit, dips are consistently ~200/20 throughout the lower parts of the unit but towards the top of the unit dips becomes nearly horizontal and there are lateral variations in bed thickness, not uncommon within river or fan deposits.

The debris flow is semiconsolidated and clast supported with cm to dm scale well-rounded clasts. The clasts are mostly black and grey limestone (95%). Other clast lithologies include black and green gneisses, jasper and distinctive yellow rock with white veins. No clear stratification can be spotted within this unit, which is characteristic of debris flows. Dips can be measured on occasional sandy interbeds within the massive debris flow. The unit is intensively tectonized.

At r-22 there is ~20 m of finer siliciclastics suggesting a temporary decrease in the energy of the depositional flow. This succession consists of sandstone (quartz arenites) and pebbly sandstones with well-rounded clasts up to 5 cm in diameter. The clasts are mostly limestone but some are metamorphic and igneous rocks. In the top portion of the unit there is a distinct violet mudstone.

### 3.3. Volcanic Conglomerate (vc)

This unit is a mixture of the Orange Debris Flow, described above with another coarse siliciclastic deposit with high volcanic clast content. Although this unit was observed only in fault contact with surrounding units, it was concluded that it lies below or within the Orange Debris Flow because parts of this unit are so similar to Orange Debris Flow. Clasts are generally angular; most of them are volcanic with a porphyritic texture and andesitic composition (hornblende, pyroxene, amphibole and quartz) (Figure 3-10). Other clasts are rock fragments.

At locality r-23 this conglomerate with volcanic clasts unconformably overlies a debris flow equivalent to the Orange Debris Flow unit (Figure 3-11). Bedded volcanic-rich conglomerate is interbedded with layers of limestone-rich debris flow. The appearance of volcanic clasts, which increase in abundance upwards, should be correlated with a major volcanic event in the area, while the reappearance of limestone-rich conglomerate should correspond to a waning of the volcanic activity. This volcanic activity may correspond to the late Miocene andesitic arc in the Aegean.

### 3.4. Red Conglomerate (rc)

This unit is characteristically a bright red color, similar to the redbeds contained within the immediately underlying basement. However, Mesozoic redbeds in the basement unit are folded, while the younger sedimentary succession is not. At locality r-24 the basement redbeds

are folded, while the overlying sediments, which are unconformable or in fault contact with the basement redbeds, are clearly bedded and shallowly dipping (Figure 3-12).

The conformable contact between the Red Conglomerate unit and the underlying Upper Conglomerate is present in the river valley at locality r-25, where there is an upward succession from coarse conglomerate through sandstone to the Red Conglomerate. In the basal part of the unit at locality r-26 the Red Conglomerate is found to be clearly bedded and includes sandstone interbeds.

### 3.5. Upper Conglomerate (uc)

This unit is generally well silicified. It is distinguished from the underlying Lower Conglomerate by its better silicification and lesser sandstone content (Figure 3-13). Due to strong cementation of its layers, this unit is very hard and is a cliff former. The highest topography in the central-northern part of the study area is comprised solely of this unit (Figure 3-14). The Upper Conglomerate is a massive rock, with no clear bedding visible, except where there are frequent sandstone interbed. It is usually grey, although at several localities is intensively red (r-27 to r-30) (Figure 3-15). The red alteration seems to coincide with layers of higher sandstone content.

This conglomerate unit is clast supported, containing well-rounded oval-shaped clasts up to several cm in diameter. The most prevalent clast material is limestone (95% in most cases). The secondary clast composition is metamorphic rock derived from the basement formations, but there are also some other rock fragments. At several localities clasts of another limestone-rich conglomerate were observed, which is an evidence of a progressive uplift or several stages of uplift. The matrix varies from clay to siliceous and the unit is highly tectonized (r-31 and r-32), as are all the units in this basin.

Around the midpoint of this unit there is a distinctive fine-grained succession several meters thick that includes limestones, sandstones and mudstones (r-33 and r-34) (Figure 3-16). Cross-stratification features indicate that the unit is not overturned (Figure 3-17).

### 3.6. Lower Conglomerate (lc)

This unit is similar to the Upper Conglomerate, but it is less silicified and has higher sandstone content. Both units contain well-rounded limestone clasts. The oval shape and size (several cm) of the limestone clasts is common to both conglomerate units. The clasts orientation shows horizontality and is consistent with the sandstone interbeds orientation. The conglomerate beds are generally matrix supported with well-sorted clasts and sandy matrix. Frequent sandstone interbeds in this conglomerate demonstrate a clear stratification (Figure 3-18). In places a red alteration is encountered (r-35), not unlike that observed in the Upper Conglomerate (Figure 3-19).

Although this unit is well stratified, there is little regularity of spacing of the conglomerate and sandy beds. Locally, the sandy beds exhibit cross-stratification. In particular, at locality r-35 cross-stratification within a better-cemented and preserved sandstone bed was observed with foresets oriented at 061/28. This indicates a paleoflow direction to the south (Figure 3-20, Figure 3-21).

The contact between the Lower and Upper Conglomerate units was encountered at r-36 (Figure 3-22) and also along the river valley from r-37 to r-38. The contact is transitional and conformable as the less compact and sandier conglomerate becomes increasingly more silicified and loses the frequent sandstone interbeds.

### 3.7. Solid Sandstone (ss)

This unit is easily distinguished from the Lower Conglomerate, which has high sandstone content but is not well cemented and contains medium to coarse grained sandstone (Figure 3-23).

The Solid Sandstone is characterized by a higher degree of cementation and by finer grain size. It is very well stratified with well-sorted sandstone beds several cm thick and frequent mudstone interbeds. At locality r-39 the mudstone beds are about 20 cm thick and the sandstone beds are about 5 cm thick. This unit exhibits soft-sediment deformation features and is not overturned. Conformable contact with the underlying Purple Debris Flow is not observed in the field but it is conjectured from the consistent dips of the two units.

**3.8. Purple Debris Flow (pdf)**

This unit is characterized by poorly-sorted large subangular clasts up to a meter in diameter. The clasts are mostly green metamorphic or igneous rocks. The unit is clast-supported with a characteristic purple clay and siliceous matrix (Figure 3-24, Figure 3-25).

**3.9. Basement (b)**

The basement in the field area consists primarily of Mesozoic carbonates. Some gneisses and schists were encountered in the northwest corner of the mapping area (Figure 4-13). At locality r-25, a variety of basement formations crop out, including metamorphosed redbeds. The redbeds are strongly folded and metamorphosed (Figure 4-17). The color of this unit is similar to the Miocene Red Conglomerate, suggesting that the Mesozoic redbeds are the source rock for the Miocene unit. The red color is a result of the oxidized state of Fe in the minerals, indicating that the protolith was deposited on dry land, probably in an area with high relief. It is typical of fluvial or alluvial deposits.

In the vicinity, there are several outcrops of the strongly brecciated dolostones on the fault plane between basement and Miocene conglomerate (Figure 4-15). They are probably faulted lenses of the basement formations that were dragged along the fault.

A cursory survey of the region beyond the map presented in Figure 3-1 shows that the basement limestones are commonly highly brecciated and even shattered, perhaps indicating

proximity to a fault (r-40). The breccias are clast-supported, with sharp-edged pure black limestone clasts of cm scale. The breccias are not well cemented and are easily crumbled. At some localities there are calcite veins filling in fractures in this tectonized unit. It is concluded that this unit exhibits tectonic brecciation.

## 3.10. Depositional sequence

From the observations presented above, we can construct the following depositional history of this part of the Limni-Istiea basin

1. The development of steep relief, probably by extensional faulting (see next section) created debris flows. The first of these to be deposited was the Purple Debris Flow. It contains predominantly igneous and metamorphic clasts, indicating a provenance in the metamorphic units of the basement. Next, the depositional flow decreased in energy and mudstones were deposited in a fluvial environment.

2. After a period of tilting the sandstone-rich limestone conglomerate was deposited, followed by silicified conglomerate. These contain highly rounded clasts indicating that the source of the sediments was farther from the basin than that of the debris flows. The source rock for these conglomerates was largely the basement carbonate units.

3. The next stage involved formation of a shallow lake, in which marl and sandstone were deposited. Following another faulting event and relief formation, an occasional debris flow also occurred. The main source for the debris flows were the basement carbonates, but as a result of a localized volcanic event the flows also contained high volcanic clast content, at least locally. The fact that most of the clasts are limestone throughout the deposition of this unit points to a uniformity of the source region.

# 4. Structure

All the units in the field area are strongly tectonized. Dominant structures include folding that is confined to the pre-basinal basement rocks, and normal faults that cut the basin sediments and in some places juxtapose basin sediments against the underlying basement. There appears to be a relative chronology that is largely related to the trend of the structures.

Filed mapping revealed what is interpreted to be three sets of faults associated with several stages of extension (Figure 4-1). They are all normal in the sense of movement and dipping in different directions. The oldest structures are the low angle north-south trending and east-dipping faults. West-east or southwest-northeast trending faults are younger. The youngest formation is the northwest-southeast trending and generally west-dipping faults. These youngest structures are best expressed in the topography and in the coastline.

The structures are described from apparently youngest (set $\alpha$) to apparently oldest (set $\delta$). The structures in each set are ordered form the most significant (1) to less significant (2 and higher). The same designations are used on the structural map (Figure 4-1) and the cross sections (Figure 4-2).

## 4.1. Northwest-southeast trending faults ($\alpha$)

Some of the more prominent structural elements in the field area are the northwest-southeast trending faults ($\alpha$1, Figure 4-1) that superimpose the Marl unit against the older sedimentary units. As is demonstrated on cross sections C, D and E (Figure 4-2c, d, and e), these structural elements are well-expressed in the local topography, consistent with the inference that they are among the youngest in the basin. The attitude of the main fault plane or of a neighboring shear zone can be measured at the strongly tectonized locality s-1, and is 153/30 and 180/25, demonstrating that the fault dips gently to the west or southwest.

There are several faults that are parallel or subparallel to the fault α1 and they probably formed during the same period of extensional deformation, constituting a bookshelf-type fault geometry within its upper plate. For example, in several localities approximately north-striking fault planes parallel fault α1, but dip towards the northeast, for example at s-2, where a fault within Lower Conglomerate is oriented 300/72 ( Figure 4-3). Another fault nearby is oriented 345/40. These secondary, east to northeast-dipping faults are located in the hanging wall of α1 and probably represent extensional deformation localized within its upper plate (Figure 4-2d, and e). Displacements on these hanging wall faults are estimated as several hundred meters.

In the southern part of the field area, east of fault α1, fault α3 superimposes the Marl formation against the basement. At locality s-3, the fault is oriented at 191/34, with slickenlines at 207/22. At the same locality another fault plane is present, oriented 140/49 with slickenlines 200/47. To the west, fault α4, inferred to be dominantly strike-slip, is observed at locality s-4 where it is oriented 153/85. This fault superimposes the Marl formation against the Orange Debris Flow (Figure 4-4).

In the northern part of the mapped area, fault α2 drops the Upper and Lower Conglomerate units against the oldest sedimentary units in the field area: the Purple Debris Flow and Solid Sandstone units. An attitude measured on this fault at locality s-5 is steep, 168/85 with slickenlines at 166/24. Another fault plane in the vicinity displays a similar orientation, 159/79 and slickenlines 336/83. The next fault to the east, α7, exposes the carbonate basement formations in its footwall. Slightly to the west of fault α7, the presence of fault α6, cutting the Upper and Lower conglomerate units, is tentatively inferred from an attitude of 162/76 measured on an apparent fault plane at s-6 as well as from the bedding inferred to be rotated into parallelism with the fault. To the northwest of fault α1, two subparallel faults α5 and α8 are inferred. The attitude on fault α5 at locality s-7 is consistent with its being a southwest dipping normal fault: 134/78 with slickenlines 324/78 (Figure 4-5, Figure 4-6).

Other approximately northeast trending faults include that observed at locality s-8, which is oriented 150/60. This appears to be a minor structure, with displacement estimated at 20 m. At s-9, an attitude of 117/60 was measured on another minor fault within the Lower Conglomerate unit. At s-10 there is a set of normal faults with cm scale displacements and orientations of 190/20 and 152/32 (Figure 4-7).

## 4.2. The southern fault system (β)

In the southwest part of the field area, between the towns of Limni and Rovies near the coast, a steep west-east trending fault β1, superimposes the Marl unit to the north against a variety of faulted basin units to the south. South of β1, the faults within the basinal units have subparallel strikes and are perpendicular to β1. These superimpose the youngest sedimentary units of the basin against each other. The westernmost of these faults, β2, dips gently east and brings up the Volcanic Conglomerate unit in the foot wall.

Fault β2 forms a basal detachment and faults β3 and β4 are the faults in the hanging wall that rotate and tilt the hanging wall blocks, hence repeating the strata of the Marl and Orange Debris Flow formations, as observed at s-11 (Figure 4-2d, Figure 4-8). Here, faults β3 and β3 cut and juxtapose the Orange Debris Flow and Marl units; all of these units are superimposed against the Volcanic Conglomerate across fault β2. All three faults end northward against β1, which appears to function as a steep tear fault accommodating extension on its south side.

At s-12 bedded Volcanic Conglomerate is faulted against the Marl unit (Figure 4-9). At this outcrop there are beds of variable volcanic clast content. Beds of the Marl unit exposed at this locality are similar to the siliciclastic succession encountered above the massive marl formation at locality s-13 and are interpreted to be correlative with that part of the section. Farther east, at s-14, a steep normal fault strikes 025/70 and superimposes sandy beds on the east against and the coarse part of the Orange Debris Flow unit. At s-15 there is mezzo-scale faulting with intense fracturing and calcite veins.

This entire package of faults, including the steep east-west trending β1, may be of the same age as the most prominent northwest-southeast trending fault in the area, α1. It is not unlikely that left-slip displacement on β1 dies out into the broad sinistral bend formed in the surface trace of α1 immediately east of β1. Alternatively, β1 and related faults may be younger than fault α1 and the bend in the trace of α1 is due to later movement on β1.

### 4.3. West-east or southwest-northeast trending faults (γ)

The most prominent of the east-west or northeast-southwest trending faults observed in the field area are the set of faults γ1, γ2, γ3 and γ4 (Figure 4-2a and b). These faults are clearly expressed in the local topography and morphology, with the highest topographic region comprised of the Upper Conglomerate unit exposed on the north, footwall side of these faults. This set of faults is cut by the northwest-southeast trending faults α described above indicating that the east-west trending faults are older. At locality s-16 shear planes oriented 060/19 and 104/32 are associated with fault γ1 (Figure 4-10). At s-17 another fault separating the basement gneisses from basin conglomerate is oriented at 093/22. At s-18, there is a fault oriented 304/60 with slickenlines 129/10 and at locality s-19 the well-exposed fault surface of fault γ4 is oriented 043/85 with slickenlines 043/43 (Figure 4-11, Figure 4-12).

In the central part of the filed area, southwest-northeast trending fault γ5 dips to the southeast and juxtaposes the Marl and Orange Debris Flow units in its hanging wall against the Upper and Lower conglomerate units in its footwall (Figure 4-2b). To the south, close to the coast, another east-west trending, apparently north-dipping fault γ6 superimposes the Marl unit in its hanging wall against the basement in the footwall.

Similarly-oriented fault planes were also observed within the Upper and Lower conglomerate units, including at s-20 a plane 070/64 with striations 275/74; at s-21 a fault plane 217/13. At the strongly tectonized locality s-1, one fault plane measured 055/49 and nearby another fault plane measured 044/71 with slickenlines 035/68.

## 4.4. Northwest and northeast regions of the field area (δ)

In the northwest corner of the field area there is a low-angle tectonic contact δ1 between the basement and the basin sedimentary units (Figure 4-13, Figure 4-2c). At locality s-22 the fault is oriented 008/19 with mullions 063/18 (Figure 4-14). Along this contact there are highly tectonized dolostone breccias (s-23, s-24), which might be extensive fault lenses caught along the normal fault (Figure 4-15).

In the northeast corner of the filed area another fault δ2 dips to the east. It must be one of the oldest structures present in this part of the basin because it is cut by southwest-northeast trending fault γ4.

## 4.5. Basement features

The pre-basinal basement is strongly tectonized and shear zones with normal sense of movement are common (Figure 4-16). Tectonism and brecciation of the sort observed here is typical for regions that have undergone extension and very shallow crustal depths. The basement units also exhibit folding that is not present in the basin deposits, for example at locality s-23 there is a strongly folded Mesozoic redbeds unit with isoclinal folds overturned to northwest (Figure 4-17, Figure 4-18). This indicates that folding occurred prior to basin deposition.

## 4.6. Extensional sequence

From the fault relations summarized above, the following sequence of extensional events can be constructed for this part of the Limni-Istiea basin:

1. Extension along northwest-southeast northeast-southwest trending, east dipping faults.

2. East-west to trending and southeast dipping faults occurred in the southern portion of the field and perhaps elsewhere. These are linked to north-south trending faults in the southern part of the field area.

3. Northwest-southeast trending faults formed, cutting the basinal deposits and basement. These are well expressed in the modern topography.

## 5. Rotation

The paleomagnetic research in the Aegean realm has been carried out extensively for about 30 years (e.g., Laj et al., 1982; Horner and Freeman, 1983; Mauritsch et al., 1995; Speranza et al., 1995; Duermeijer et al., 2000; Kissel et al., 2003; Kondopoulou, 2000; van Hinsbergen et al., 2005). The results show significant clockwise rotations along the Hellenic arc. Several studies (Kissel and Laj 1988, Speranza et al. 1995; Kissel et al., 2003) suggested that this rotation occurred in two phases of approximately 25° each, the first one in the middle to late Miocene and the second in the Plio-Pleistocene. Van Hinsbergen et al. (2005) confirm the rotation of ~50° since the middle Miocene in western and central Greece, including Evia (Figure 5-1). Previously published results indicate clockwise rotation in the region of northern Evia of about 50° since the late Miocene (Laj et al., 1982; Kissel and Laj, 1988; Speranza et al., 1995; Kissel et al., 1995).

There are only few results published from northern or central Evia. Laj et al. (1982) sampled Miocene sediments of the northern Evia, but the sample was discarded form the analysis due to very low magnetization. Kissel et al. (1986) give results of 48° clockwise rotation in lacustrine marls (dated as at most Upper Miocene) in Kymi in central Evia. She cites magnetic inclination measurements of 35°, which would indicate a significant northward movement of Evia since the Miocene. Morris (1995) sampled in Kymi and found a clockwise rotation of 51° in 13-15 Ma andesites and 19° in Miocene marls. He gives magnetic inclinations of about 40° for both localities, which is again southward of the present latitude of Evia.

Marl is the youngest rock unit present in the field area, except for the Quaternary alluvium. It was deposited after the faulting event that produced west-east trending and south-

dipping structures in the basin but predates the last faulting event identified in the basin which produced the northwest-southeast trending and west-dipping faults. The paleomagnetic analysis, described below, reveals a clear modern field overprint and a primary magnetization with 18° clockwise rotation since the Miocene.

## 5.1. Samples

Samples collected for this study come from seven localities (A through G) within the Marl unit in the vicinity of Limni (Figure 5-2). At locality A, a thick succession of massive marl was exposed and easily accessible, which made it possible to collect from as many as nine sites (beds). At other localities only two or three sites could be sampled. The total number of 75 cores was collected with the use of a water-cooled, gasoline-powered portable drill.

Each core was split into 2 to 4 measurable samples. From the total number of 200 samples, 21 were set aside for the rock magnetism analysis and 179 were used in the thermal demagnetization analysis. Additionally, all four samples from site F1 were removed from the thermal demagnetization measurements after heating them to 295°C due to inconclusive data. Among the drill cores, the prevalent lithology is marl, but there are also limestones and sandstones (Table 5-1).

## 5.2. Rock magnetism analysis

The lab work for this part was done using a Superconducting Rock Magnetometer 755 by 2G Enterprises housed in the MIT Paleomagnetism Laboratory (web.mit.edu/paleomag). Associated with the magnetometer are an alternating field (AF) degausser, isothermal remanent magnetization (IRM) acquisition, anhysteretic remanent magnetization (ARM) acquisition and susceptibility measuring equipment. These are integrated with a 200-sample automated robotic measurement system (Kirschvink et al. 2008). ARM and IRM analyses were done for 8 samples, including at least one from each locality. Additionally, hysteresis loops analysis was performed

for five samples using a vibrating sample magnetometer housed in the MIT Department of

Materials Science and Engineering.

**Table 5-1.** Paleomagnetic
samples

| Locality | Site | No of cores | Lithology | Analysis performed | | |
|---|---|---|---|---|---|---|
| | | | | Rock magnetism | Hysteresis | Thermal demagnetization |
| A | A1 | 3 | marl | * | * | * |
| | A2 | 3 | marl | * | * | * |
| | A3 | 4 | marl | | | * |
| | A4 | 3 | marl | | | * |
| | A5 | 3 | marl | | | * |
| | A6 | 3 | marl | | | * |
| | A7 | 2 | marl | | | * |
| | A8 | 2 | marl | | | * |
| | A9 | 3 | marl | | | * |
| B | B1 | 3 | marl | * | * | * |
| | B2 | 3 | marl | | | * |
| | B3 | 3 | marl | | | * |
| C | C1 | 3 | marl | | | * |
| | C2 | 3 | sandstone | * | | * |
| D | D1 | 3 | limestone | | | * |
| | D2 | 3 | marl | * | * | * |
| | D3 | 3 | marl | | | * |
| E | E1 | 3 | marl | * | * | * |
| | E2 | 3 | marl | | | * |
| | E3 | 3 | marl | | | * |
| F | F1 | 3 | limestone | | | |
| | F2 | 3 | marl | | | * |
| | F3 | 3 | marl | * | | * |
| G | G1 | 4 | limestone | | | * |
| | G2 | 3 | limestone | * | | * |

## 5.2.1. ARM (anhysteretic remanent magnetization)

ARM is acquired artificially when a rock is subjected to an AF superposed on a DC bias

field. Grains with coercivity lower than the peak oscillating field will flip along with the field. As

the AF decays below the coercivity of certain grains, they will lock in one direction. Statistically,

half of them will freeze in one direction, and the other half in the opposite, contributing to zero

remanence in a pure AF. However, when a DC bias field is applied as well, there will be

preference in the remagnetized grains to align with the DC field direction. This magnetization is the ARM (Butler, 1998).

ARM acquisition as a function of DC bias field for the eight samples is presented in Figure 5-3. This analysis shows that the samples are moderately interacting, as they lie in the lower portion of the graph (Cisowski, 1981).

## 5.2.2. IRM (isothermal remanent magnetization)

In this experiment, the samples were exposed to a strong magnetic field at room temperature. Ferromagnetic grains with coercivities less than the applied field flip to align with the field, resulting in a gain in the magnetic remanence in that direction (Tauxe, 2005).

Figure 5-4 shows the acquisition and demagnetization curves for the 8 samples. It is clear that generally the samples are not saturated even by the highest applied field (the only exception is sample A2). Their coercivity of remanence ranges from ~35-55 mT. The magnetization of these samples is therefore likely dominated by high coercivity minerals like hematite and greigite (Roberts, 1995; Peters and Dekkers, 2003) (Table 5-2). We suggest that for sample A2, the dominant magnetic mineral is magnetite, since it is saturated by the field of 300 mT.

**Table 5-2.** Magnetic minerals parameters

| Mineral | Formula | Characteristic temperature | Typical coercivity |
|---------|---------|----------------------------|--------------------|
| Magnetite | $Fe_3O_4$ | Curie temperature = 580°C | 10's of mT |
| Hematite | $\alpha Fe_2O_3$ | Neel temperature = 675°C | vary widely and can be 10's of T |
| Greigite | $Fe_3S_4$ | Maximum unblocking temperature = ~330°C *Breaks down to magnetite: ~270-350°C | 60→> 100 mT |

(from Roberts, 1995; Peters and Dekkers, 2003)

### 5.2.3. Lowrie-Fuller test

The Lowrie-Fuller test compares the ARM and IRM demagnetization curves for various applied fields. It is a weak diagnostic tool, especially for the data where the ARM and IRM curves lie close to each other, as is the case with the samples analyzed in this study.

In the Lowrie-Fuller test (Xu and Dunlop, 1995), if the ARM demagnetization curve falls below the IRM demagnetization curve, the specimen is multidomain (MD). For most of the samples the two curves are very close to each other, but the ARM is slightly smaller than IRM (Figure 5-5). This suggests a pseudo-single domain grain size. Only for G2 ARM is significantly greater than IRM, such that G2 could be predominantly single domain.

### 5.2.4. IRM derivative

Curves presented in Figure 5-6 are generated by taking the derivative of the IRM demagnetization (AF) and acquisition (Acq) curves. It is clear that all of the samples exhibit a bimodal coercivity distribution. This is indicative of at least 2 different superposed coercivity spectra (Tauxe, 2005). All of the samples have one of the peaks at 40mT which corresponds to the coercivity of magnetite. The other peak, which occurs around 80 mT, could be associated with hematite of greigite.

### 5.2.5. Day plots

The Day plot gives the ratio of the induced magnetization and the saturation magnetization ($M/M_s$) as a function of the ratio of coercivity of remanence to coercivity (Dunlop, 2002a, b). These parameters are derived from hysteresis loops and the IRM acquisition and demagnetization data described above. This is probably the most robust indicator of grain size (Figure 5-7).

## 5.3. Thermal demagnetization

In thermal demagnetization, a sample is heated to an elevated temperature ($T_{demag}$) and then cooled to room temperature in a zero magnetic field. All grains with blocking temperature ($T_b$; temperature at which grain becomes superparamagnetic) become demagnetized. The only magnetization left in the sample is the NRM carried by the minerals with blocking temperature higher than $T_{demag}$. Due to the fact that there is a strong correlation between the temperature and the coercivity of a grain (Tauxe, 2005); the higher the sample is heated up, the smaller the amount of magnetized low coercivity grains. It is the high coercivity grains that carry the primary NRM. Thus, in the process of gradual heating and measuring the magnetic vector orientation, any secondary overprints acquired low coercivity grains are removed and the only remaining magnetization is the NRM that the sedimentary rock recorded during the deposition.

A thermal demagnetizer with controlled atmosphere and paleointensity coil by ASC Scientific was used to heat the samples in 50, 25 or 15 degree intervals. The analysis began with 179 samples. Samples A were heated up to 430°C and all the other were heated up to 415°C, with the exclusion of F1 samples (removed from the experiment after 295°C). It was found that around 400°C the samples were almost completely demagnetized (Figure 5-8) at which point the experiment was stopped. It is therefore conjectured that if there is magnetite, it is not a prevalent magnetic mineral in any sample (it has $T_c$ of 580°C).

## 5.3.1. Preliminary analysis

During the beginning stages of the analysis of the data, most of the samples exhibited a clear low temperature component (LT) that demagnetized between the temperatures of 50°C and 150-200°C. Above that temperature, another direction thermal demagnetization isolated a high temperature component (HT) (Figure 5-9).

### 5.3.2. The LT component

For all samples except for those from locality E, the LT component is close to the current field in Greece (declination = 3.3°, inclination = 55.4°; Table 5-3; Figure 5-10). Samples from locality E have LT components that have declinations that are rotated counterclockwise by about 44° with respect to the present field. We conclude that the LT component for all samples but locality E is the contemporary magnetic field overprint. The result for E remains inconclusive.

### 5.3.3. The HT component and rotation

Our analysis of the HT component had 2 parts because it was clear that data from locality A are significantly different from those of the rest of the basin. At locality A, the declination and the inclination of the measured vector are 54.3° and 57.2°, which is equivalent to about 54.3° of clockwise rotation with respect to the present field (Table 5-4, Figure 5-11).

Locality G was excluded from the rotation analysis due to the fact that these data were inconsistent with the rest of the basin. The data from B, C, D, E and F (henceforth referred to as BCDEF) are consistent with each other and give a declination of 18.1°, and inclination of 53.8°. Since these data cover a larger area than those of locality G and are consistent, it is concluded that they are more representative of paleomagnetization in the basin. Therefore, the representative amount of rotation for this part of Limni-Istiea basin is 18.1° clockwise.

The quality of the HT results is ascertained by the reversal and fold test, which are passed by data from A and BCDEF. The reversals test is based on the fact that the normal and reversed field vector directions are antiparallel. A characteristic remanent magnetization (ChRM) passes the reversals test if the mean direction of the normal polarity is within error antiparallel to the reverse polarity directions (Butler, 1998). The data passes the quality factor C reversal test of McFadden and McElhinny (1990) with site A8 excluded (otherwise the test is negative). Samples BCDEF pass the C reversal test when D1 is excluded. Exclusion of sites A8 and D1 is justified by

**Table 5-3.** LT component

| Locality | Nc | Decl TC | Incl TC | Decl IS | Incl IS | k | α95 |
|---|---|---|---|---|---|---|---|
| all mean | 21 | 90 | 0 | 360 | 55.7 | 35.2 | 5.4 |
| A mean | 9 | 24.4 | 39 | 9.2 | 53 | 90.2 | 5.4 |
| A1_LT | 6 | 26.4 | 36.8 | 12.9 | 51.6 | 117 | 6.2 |
| A2_LT | 8 | 28.1 | 25.2 | 19.8 | 40.9 | 50.7 | 7.9 |
| A3_LT | 8 | 27.1 | 35.9 | 14.3 | 50.8 | 467 | 2.6 |
| A4_LT | 4 | 19.2 | 38 | 3.7 | 50.6 | 24.5 | 18.9 |
| A5_LT | 8 | 22.3 | 34.1 | 9.4 | 47.9 | 400 | 2.8 |
| A6_LT | 10 | 30.3 | 39.7 | 16.2 | 55.2 | 115 | 4.5 |
| A7_LT | 4 | 30.3 | 51.7 | 6.6 | 66.3 | 35.6 | 15.6 |
| A8_LT | 4 | 15.1 | 45 | 354.3 | 55.7 | 9.3 | 31.9 |
| A9_LT | 4 | 19.7 | 43.8 | 0.4 | 56.1 | 193 | 6.6 |
| BCDFG mean | 8 | 90 | 0 | 1.2 | 51.8 | 82.4 | 6.1 |
| B1_LT | 6 | 28 | 46.4 | 90 | 0 | 85.7 | 9.4 |
| B2_LT | 6 | 19.7 | 55.6 | 90 | 0 | 65.1 | 10.8 |
| B3_LT | 7 | 44.2 | 41.5 | 90 | 0 | 213 | 5 |
| C1_LT | 8 | 10.6 | 55 | 6.2 | 52.6 | 169 | 4.3 |
| C2_LT | 7 | 3.5 | 56 | 359.4 | 53.2 | 316 | 3.4 |
| D1_LT | 8 | 355.1 | 60.2 | 347.9 | 48.3 | 9.6 | 18.8 |
| D2_LT | 8 | 23.8 | 61.6 | 8.6 | 52.8 | 209 | 3.8 |
| D3_LT | 4 | 39 | 73.9 | 8.8 | 66.3 | 7.5 | 36 |
| F2_LT | 7 | 6.9 | 18 | 359.4 | 45.7 | 299 | 3.5 |
| F3_LT | 9 | 1.2 | 15.5 | 353 | 41.9 | 300 | 3 |
| G1_LT | 10 | 239.9 | -61.4 | 196.4 | -75 | 3.5 | 30.3 |
| G2_LT | 7 | 27.2 | 36 | 12.1 | 51.9 | 9.6 | 20.5 |
| E mean | 3 | 320 | 37.1 | 316.2 | 59.9 | 85.4 | 13.4 |
| E1_LT | 8 | 311.7 | 33.9 | 304.4 | 55.8 | 50.4 | 7.9 |
| E2_LT | 9 | 328 | 43.8 | 329.5 | 66.7 | 86.4 | 5.6 |
| E3_LT | 6 | 321.3 | 33.2 | 318.9 | 56.1 | 58.6 | 8.8 |

**Table 5-4.** HT component

| Locality | Nc | Decl TC | Incl TC | Decl IS | Incl IS | k | α95 | Pol | Rot | Sense |
|---|---|---|---|---|---|---|---|---|---|---|
| A mean | 8 | 54.3 | 57.2 | 42.1 | 76.6 | 51.2 | 7.8 | N | 54 | cw |
| A1_HT | 6 | 233 | -54.6 | 221.6 | -73.9 | 154 | 5.4 | R | 53 | cw |
| A2_HT | 8 | 224.2 | -57.7 | 200.4 | -75.3 | 492 | 2.5 | R | 44 | cw |
| A3_HT | 8 | 253.3 | -55.1 | 265.4 | -74.4 | 387 | 2.8 | R | 73 | cw |
| A4_HT | 6 | 32.5 | 49.3 | 12.1 | 64.7 | 8.4 | 24.5 | N | 33 | cw |
| A5_HT | 8 | 236.1 | -63 | 218.5 | -82.5 | 308 | 3.2 | R | 56 | cw |
| A6_HT | 10 | 268.4 | -53.3 | 290.8 | -69.7 | 7.8 | 18.4 | R | 88 | cw |
| A7_HT | 4 | 39.6 | 61 | 4.7 | 76.9 | 23.4 | 19.4 | N | 40 | cw |
| A8_HT | 4 | 2.3 | 44 | 341.4 | 50.7 | 8.3 | 34 | N | 2 | cw |
| A9_HT | 4 | 47.7 | 53.3 | 32.6 | 71.9 | 142 | 7.7 | N | 48 | cw |
| BCDEF mean | 12 | 18.1 | 53.8 | 90 | 0 | 76.3 | 5.3 | N | 18 | cw |
| B1_HT | 6 | 178.6 | -55.7 | 150.8 | -44.5 | 197 | 4.8 | R | 1 | ccw |
| B2_HT | 6 | 196.4 | -55.4 | 162.8 | -50.6 | 79.6 | 7.6 | R | 16 | cw |
| B3_HT | 7 | 190.5 | -62.6 | 151.1 | -53.7 | 92.6 | 6.3 | R | 11 | cw |
| C1_HT | 8 | 20.5 | 54.8 | 15.6 | 53 | 40.7 | 8.8 | N | 21 | cw |
| C2_HT | 7 | 10.4 | 58.6 | 5.4 | 56.2 | 46.8 | 8.9 | N | 10 | cw |
| D1_HT | 8 | 310 | 67.5 | 316.1 | 54.9 | 3.8 | 32.6 | N | 130 | cw |
| D2_HT | 8 | 26.4 | 53.2 | 14.4 | 45.1 | 13.7 | 15.5 | N | 26 | cw |
| D3_HT | 8 | 30.2 | 46.7 | 20 | 39.6 | 22 | 12.1 | N | 30 | cw |
| E1_HT | 8 | 198.1 | -40.1 | 219.3 | -51 | 287 | 3.3 | R | 18 | cw |
| E2_HT | 7 | 202.6 | -56.4 | 241.7 | -62.5 | 14.2 | 16.6 | R | 23 | cw |
| E3_HT | 6 | 3.5 | 48.2 | 30.2 | 63.3 | 43.8 | 10.2 | N | 4 | cw |
| F2_HT | 7 | 196.5 | -57.9 | 134.8 | -84.5 | 62.8 | 7.7 | R | 17 | cw |
| F3_HT | 9 | 201.8 | -59.7 | 121.9 | -87.7 | 233 | 3.4 | R | 22 | cw |
| G1_HT | 10 | 103.6 | 15.9 | 106 | 36.3 | 6.8 | 20.1 | N | 104 | cw |
| G2_HT | 7 | 88.9 | 38 | 101.5 | 57 | 6 | 27 | N | 89 | cw |

c=number of conclusive samples, decl=declination, incl=inclination, TC=tilt corrected, IS=in situ, k=Fisher'sprecision parameter, α95=95% cone of confidence, pol=polarity, rot=amount of rotation, sense=sense of rotation (cw=clockwise, ccw=counterclockwise)

the large uncertainties of these results (α95). This suggests that the secondary LT overprint was effectively removed during thermal demagnetization. It is concluded that this ChRM is a primary NRM, since the normal and reversed polarity sites conform to stratigraphic layering (Butler, 1998).

If a ChRM was acquired before the folding occurred, the directions of ChRM on opposite limbs are dispersed when plotted in the in situ coordinates. In the case of the data from this analysis, there is no fold per se, but there is a difference in dip between localities caused by local faulting and tilting. After applying the tilt correction, the directions converge (Butler, 1998). In the case of this data, clustering increases after the application of the structural correction (Figure 5-11d) and the McElhinny (1964) fold test is passed at 99% confidence.

### 5.3.4. Paleolatitude

In both cases, A and BCDEF, the paleolatitudes are very similar to the present latitude of the site (Figure 5-12). It is concluded that the data are of very good quality. Also, it is concluded that the recorded ChRM is not affected by the compression and tilting of the sediments during subsidence. Possibly, the mineral that recorded it was created at a later stage in the diagenesis, when the sediments were already compressed, which could point to greigite as the primary magnetic mineral in the analyzed samples. The greigite hypothesis is supported by the rock magnetism analysis, which showed that the primary magnetic mineral is a mineral with coercivity spectrum lower than magnetite, and greigite falls into this group. However, given that the magnetization acquisition time of authigenic greigite is less well-constrained than detrital remanence, it will be important to further examine this issue.

### 5.4. Summary

The results of the thermal demagnetization analysis are reliable, which is supported by the fact that the data passes the reversals and fold tests as well as by the fact that the derived

paleolatitude results are consistent with the hypothesis of southward motion of Evia since Miocene. It is concluded that the representative rotation for the field area is 18° clockwise since the Miocene. The rotation derived at one locality of 54° is considered to be anomalous.

The rotation of 18° is not consistent with the published results since the Miocene in this area (e.g. van Hinsbergen, 2005), which are ~50° for Evia and eastern Greece. If this higher amount of rotation is the correct, this could mean that the Marl unit is in fact younger than the Miocene and this would correspond to a smaller rotation. Dating of the volcanic ash collected during this study should verify that.

## 6. Interpretation

### 6.1. Sequence of events

Based on the stratigraphy and the structural features identified during the field mapping, the following geologic history of the southern portion of the Limni-Istiea basin may be inferred:

1. Initial relief formation, probably by first stages of extensional faulting that are not exposed in the field area.

2. Deposition of the debris flow (pdf) and then sandstones and mudstones (ss) in a fluvial environment.

3. Tilting.

4. Further deposition of thick limestone-rich conglomerates in fluvial environment (lc, uc, rc).

5. Faulting (δ) and relief formation, tilting.

6. Shallow lake formation and deposition of marl (m) intermitted by the debris flow events (odf, vc).

7. Faulting (γ) and tilting.

8. Faulting (β and α) and tilting.

Because the Marl unit is interpreted to be older than faulting event γ, the age of Marl would provide the upper bound on the age of faulting event γ. This date would also provide the lower bound on the age of faulting δ, which predated the deposition of Marl. As a follow-up of this study the volcanic ashes collected within the unit of Marl will be dated and integrated in the interpretation.

## 6.2. Regional extension

Faulting stages β and α are consistent with the most recent regional extensional events, which include the bounding faults of the North Evoikos Gulf. Faulting γ is consistent with the orientation of the northwest-southeast or southwest-northeast trending high-angle faults of the late Pliocene to Quaternary. The oldest structures, δ, might represent the earlier stage of extension, characterized by the low angle detachment faults. They may be associated with the southwest-northeast trending and south-dipping detachment just on the north coast of Evia.

The sequence of the local extensional events is consistent with the various stages of the regional extension within the Central Hellenic shear zone, as detailed in the Tectonic Setting chapter. That, in addition to the presence of southwest-northeast trending structures with a huge strike-slip component, indicates that the mapped area is under influence of the Central Hellenic shear zone as well as of the North Anatolian fault stress regimes.

## 6.3. Regional rotation

Since the rotations found in most localities are consistent with each other and it is not obvious which faults would have accommodated this large amount of rotation it is inferred that this rotation was accommodated by faults that are not in the field area. The result of this study, clockwise rotation of northern Evia by 18°, is not consistent with previously published results. This might indicate that the sampled Marl unit is younger than the late Miocene age or might

indicate that published results of ~50° clockwise rotation since late Miocene are too large (van Hinsbergen et al., 2005) (Figure 5-1).

## 6.4. Conclusion

Mapping reveals local extensional structures that are consistent with the regional extensional history. The region shows features consistent with the orientation of structures observed within the Central Hellenic shear zone as well as at the western end of the North Aegean trough system. Paleomagnetic analysis gives a clockwise rotation of 18°. If the inferred age of the Marl unit is correct, this is a much smaller rotation than indicated by previously published results. Work planned for the future includes dating of ash samples from the Marl section and the conglomerates section, which will provide a date on the δ faulting, on the paleomagnetically-determined rotations, and give lower bound for the age of the older extension in the Limni basin.

## Acknowledgements

There are many people who helped me in many ways since I started working on this thesis. First and foremost, I would like to thank Wiki Royden, who made this project possible in the first place and supported and believed in me along the way. Kyle Bradley was an invaluable help every step of the way. I would like to thank Clark Burchfiel for coming to the field with me and for being there for me in the thesis defense committee. I would like to thank other people who have been with me in the field: Dimitris and Maria Papanikolaou, Manolis Vassilakis and Paul Myrow. I appreciate the help of Ben Weiss, whose lab I used and who read my paleomagnetic chapter and contributed valuable remarks. Thanks to Sonia Tikoo and Laurent Carporzen form Ben Weiss' lab, with whom I shared the equipment and who made it an enjoyable experience.

Thanks to the departmental staff: Kerin Willis, who helped me a lot with the paperwork and organization of my field season and Vicki McKenna and Carol Sprague form the educational office, who patiently answered my questions. I would like to thank some of my students of the fall 2008 12.002 class and spring 2009 12.001, who brightened my year and gave me enthusiasm for my thesis work.
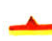
Last but not least, I would like to thank my parents and siblings. My sister Asia and my brother Piotr were great field assistants. Without their support nothing would be possible.

# References

Butler, R. F., 1998. Paleomagnetism: Magnetic Domains to Geologic Terranes. Electronic Edition.

Cisowski, S., 1981. Interacting vs. non-interacting single domain behavior in natural and synthetic samples. *Physics of the Earth and Planetary Interiors*, 26: 56-62.

Duermeijer, C.E., Nyst, M., Meijer, P.Th., Langereis, C.G., Spakman, W., 2000. Neogene evolution of the Aegean arc: paleomagnetic and geodetic evidence for a rapid and young rotation phase. *Earth and Planetary Science Letters*, 176: 509-525.

Dunlop, D.J., 2002. Theory and application of the Day plot (Mrs/Ms versus Hcr/Hc), 1. Theoretical curves and tests using titanomagnetite data. *Journal of Geophysical Research*, 107 (B3), 2056, 10.1029/2001JB000486.

Dunlop, D.J., 2002. Theory and application of the Day plot (Mrs/Ms versus Hcr/Hc), 2. Application to data for rocks, sediments, and soils. *Journal of Geophysical Research*, 107 (B3), 2057, 10.1029/2001JB000487.

Hirn, A., Nicolich, R., Gallart, J., Laigle, M., Cernobori L., ETNASEIS Scientific Group, 1997. Roots of Etna volcano in faults of great earthquakes. *Earth and Planetary Science Letters*, 148: 171-191.

Homer, F. and Freeman, R., 1983. Palaeomagnetic evidence from pelagic limestones for clockwise rotation of the Ionian zone, western Greece. *Tectonophysics, 98:* 11-27.

Ioakim, C., Rondoyanni, T., Mettos, A., 2005. The Miocene Basins of Greece (Eastern Mediterranean) from a palaeoclimatic perspective. *Revue Paléobiol.* 24 (2): 735-748.

Katsikatsos, G., Kounis, G., Fytikas, M., Mettos, A., Vidakis, M., 1980. Geological map of Greece, Limni, Sheet 1 : 50,000. IGME Publ Dept, Athens.

Katsikatsos, G., Mettos. A., Vidakis, M., 1984. Geological map of Greece, Istiea, Sheet 1 : 50,000. IGME Publ Dept, Athens.

Kirschvink, J.L., Kopp, R.E., Raub, T.D., Baumgartner, C.T., Holt, J.W., 2008. Rapid, precise, and high-sensitivity acquisition of paleomagnetic and rock-magentic data: development of a low-noise automatic sample changing system for superconducting rock magnetometers. *Geochemistry, Geophysics and Geosystems*, 9, Q05Y01, doi:10.1029/2007GC001856.

Kissel, C. and Laj, J., 1988. The Tertiary geodynamical evolution of the Aegean arc: a paleomagnetic reconstruction. *Tectonophysic, 146:* 183-201.

Kissel, C., Laj, C., Poisson, A., Görür, N., 2003. Paleomagnetic reconstruction of the Cenozoic evolution of the Eastern Mediterranean. *Tectonophysics*, 362: 199– 217.

Kondopoulou, D., 2000. Palaeomagnetism in Greece: Cenozoic and Mesozoic components and their geodynamic implications. *Tectonophysics*, 326: 131–151.

Laj, C., Jamet, M., Sorel, D., Valente, J.P., 1982. First paleomagnetic results from Mio-Pliocene series of the Hellenic sedimentary arc. *Tectonophysics, 86: 45-67.*

Mauritsch, H.J., Scholger, R., Bushati, S.L., Ramiz, H., 1995. Palaeomagnetic results from southern Albania and their significance for the geodynamic evolution of the Dinarides, Albanides and Hellenides. *Tectonophysics*, 242: 5-18.

McClusky, S., Balassanian, S., Barka, A., Demir, C., Ergintav, S., Georgiev, I., Gurkan, O., Hamburger, M., Hurst, K., Kahle, H., Kastens, K., Kekelidze, G., King, R., Kotzev, V., Lenk, O., Mahmoud, S., Mishin, A., Nadariya, M., Ouzounis, A., Paradissis, D., Peter, Y., Prilepin, M., Reilinger, R., Sanli, I., Seeger, H., Tealeb, A., Toksöz, M.N., and Veis, G., 2000. Global Positioning System

constrains on plate kinematics and dynamics in the eastern Mediterranean and Caucasus. *J. Geophys. Res.*, 105(B3): 5695-5719.

McElhinny, M. W., 1964. Statistical significance of the fold test in palaeomagnetism. *Geophys. 1. R. astr. Soc.*, 8: 338-340.

McFadden, P.L., and McElhinny, M.W., 1990. Classification of the reversal test in paleomagnetism. *Geophysical Journal International*, 103: 725–729.

Mettos, A., Rondogianni, Th., Ioakim, Ch., Papadakis, I., 1992. Evolution geodynamique et reconstruction paleoenvironnementale des basins Neogenes–Quaternaires de la Grece centrale. *Paleontologia i Evolucio*, 24–25, 393–402.

Morris, A., 1995. Rotational deformation during Palaeogene thrusting and basin closure in eastern central Greece: palaeomagnetic evidence from Mesozoic carbonates. *Geophys. J. Int.*, 121: 827-847.

Palyvos, N., Bantekas, I., Kranis, H., 2006. Transverse fault zones of subtle geomorphic signature in northern Evia island (central Greece extensional province): An introduction to the Quaternary Nileas graben. *Geomorphology*, 76: 363–374.

Papanikolaou, D.J., Royden, L.H., 2007. Disruption of the Hellenic arc: Late Miocene extensional detachment faults and steep Pliocene-Quaternary normal faults – Or what happened at Corinth? *Tectonics*, 26, TC5003.

Peters, C., Dekkers, M.J., 2003. Selected room temperature magnetic parameters as a function of mineralogy, concentration and grain size. *Physics and Chemistry of the Earth*, 28: 659–667.

Royden, L.H. and Papanikolaou, D.J., 2009. Slab Segmentation and Late Cenozoic Disruption of the Hellenic Arc. *In preparation*.

Speranza, F., Islami , I., Kissel, C., Hyseni, A., 1995. Paleomagnetic evidence for Cenozoic clockwise rotation of the external Albanides. *Earth and Planetary Science Letters*,129: 121-134.

Tauxe, L., 2005. Lectures in Paleomagnetism. Electronic Edition.
http://earthref.org/MAGIC/books/Tauxe/2005/ (May 30, 2005)

van Hinsbergen, D.J.J., Langereis, C.G., Meulenkamp, J.E., 2005. Revision of the timing, magnitude and distribution of Neogene rotations in the western Aegean region. *Tectonophysics*, 396: 1 –34.

Zijderveld, J.D.A., 1967. A.c. demagnetization of rocks: analysis of results. *Methods in Paleomagnetism*. Elsevier, Amsterdam, 254-286.
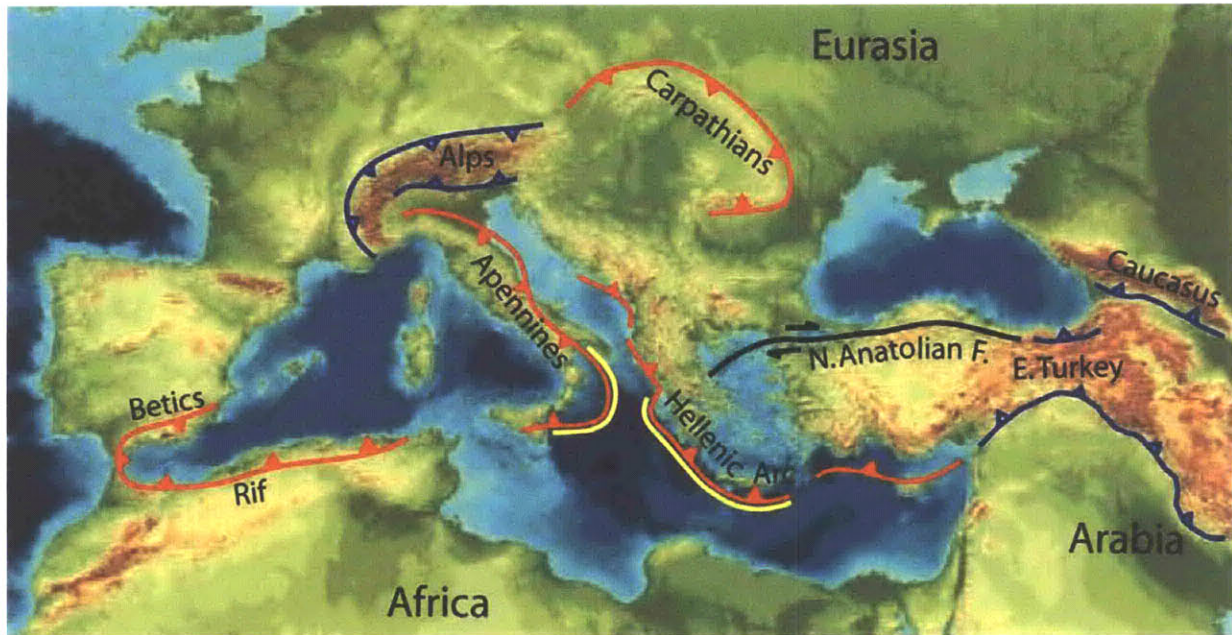
**Figure 1-1.** Map showing the main tectonic boundaries of the Mediterranean region (modified after Royden, 1993)

# GPS velocities, relative to Eurasia (McCluskey et al., 2000)



CHSZ=Central Hellenic Shear Zone          WASZ=West Anatolian Shear Zone
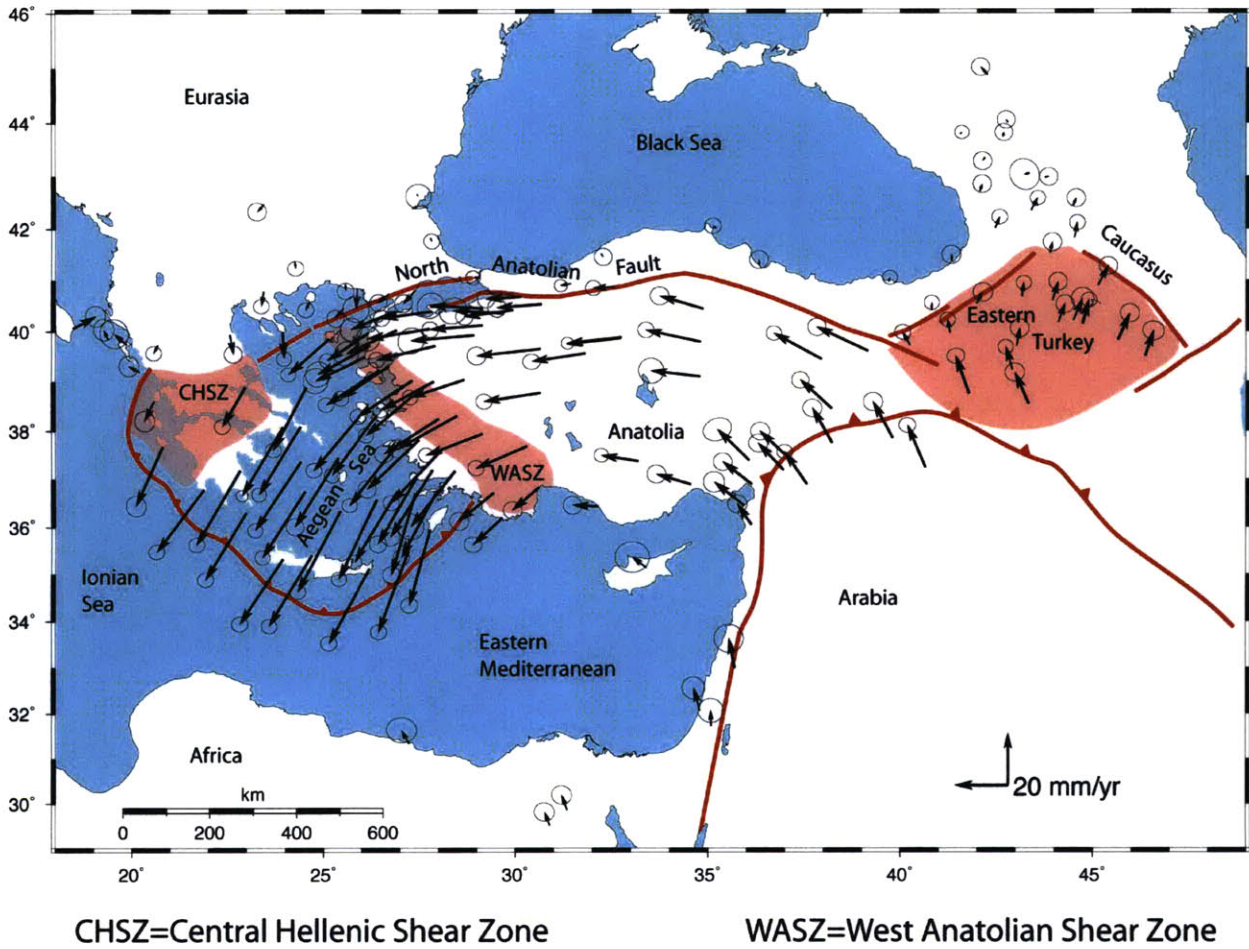
**Figure 1-2.** Convergence of Eurasian and African plates
Arrows indicate GPS velocities of the Aegean microplate relative to Eurasia.
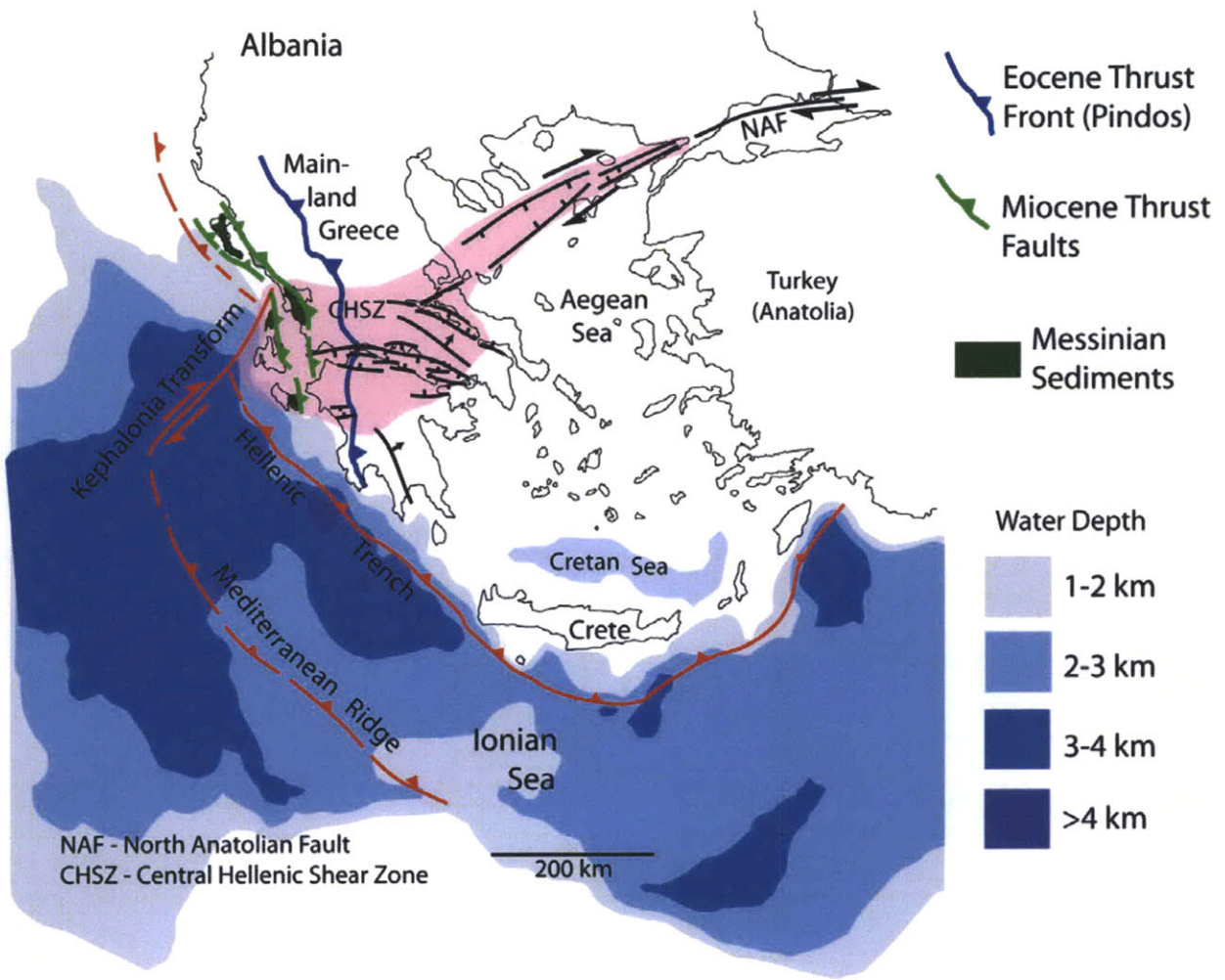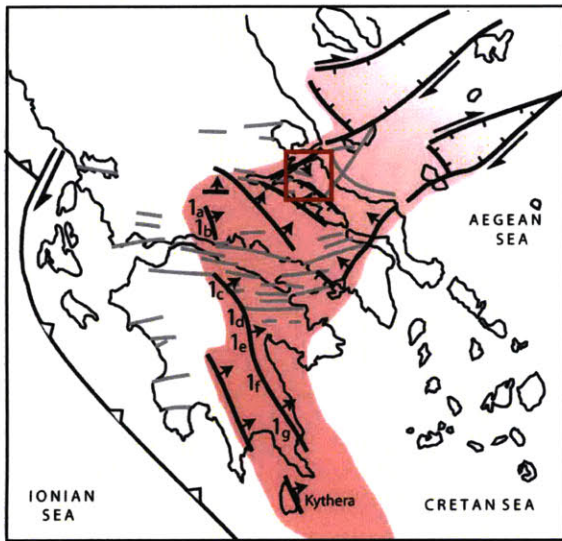(from McClusky et al., 2000)

**Figure 1-3.** Central Hellenic shear zone and Kephalonia Transform fault
Kephalonia Transform fault offsets Hellenic Trench right-laterally by about 100 km. Central
Hellenic shear zone may be considered an eastern extrapolation of the North Anatolian fault.
(from Papanikalaou and Royden, 2007)
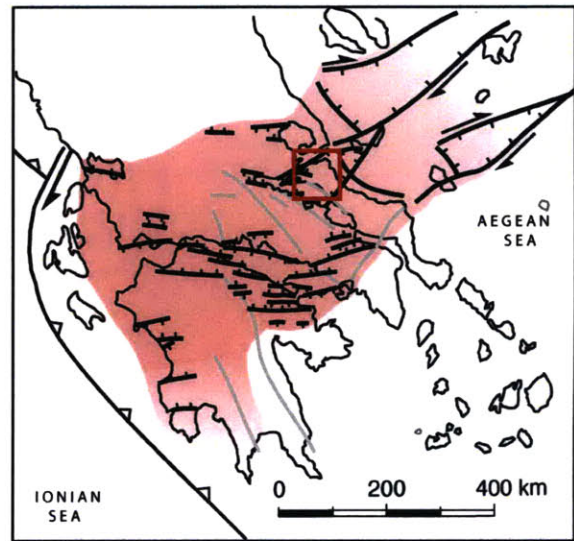
**Figure 2-1.** Neogene extensional stages within the Central Hellenic shear zone
Active faults are depicted in black. The Limni-Istiea basin is outlined in red.
(form Papanikolaou and Royden, 2007)

**Figure 3-1.** Geologic map

41

DEPOSITION                                                              TECTONIC EVENTS

Alluvium                                                                faulting ($\gamma$, $\beta$ and $\alpha$)

Marl

Orange Debris Flow
Volcanic Conglomerate                                                   faulting ($\delta$) and tilting

Red Conglomerate

Upper Conglomerate

Lower Conglomerate

Solid Sandstone                                                         tilting

Purple Debris Flow

Basement                                                                initial relief formation
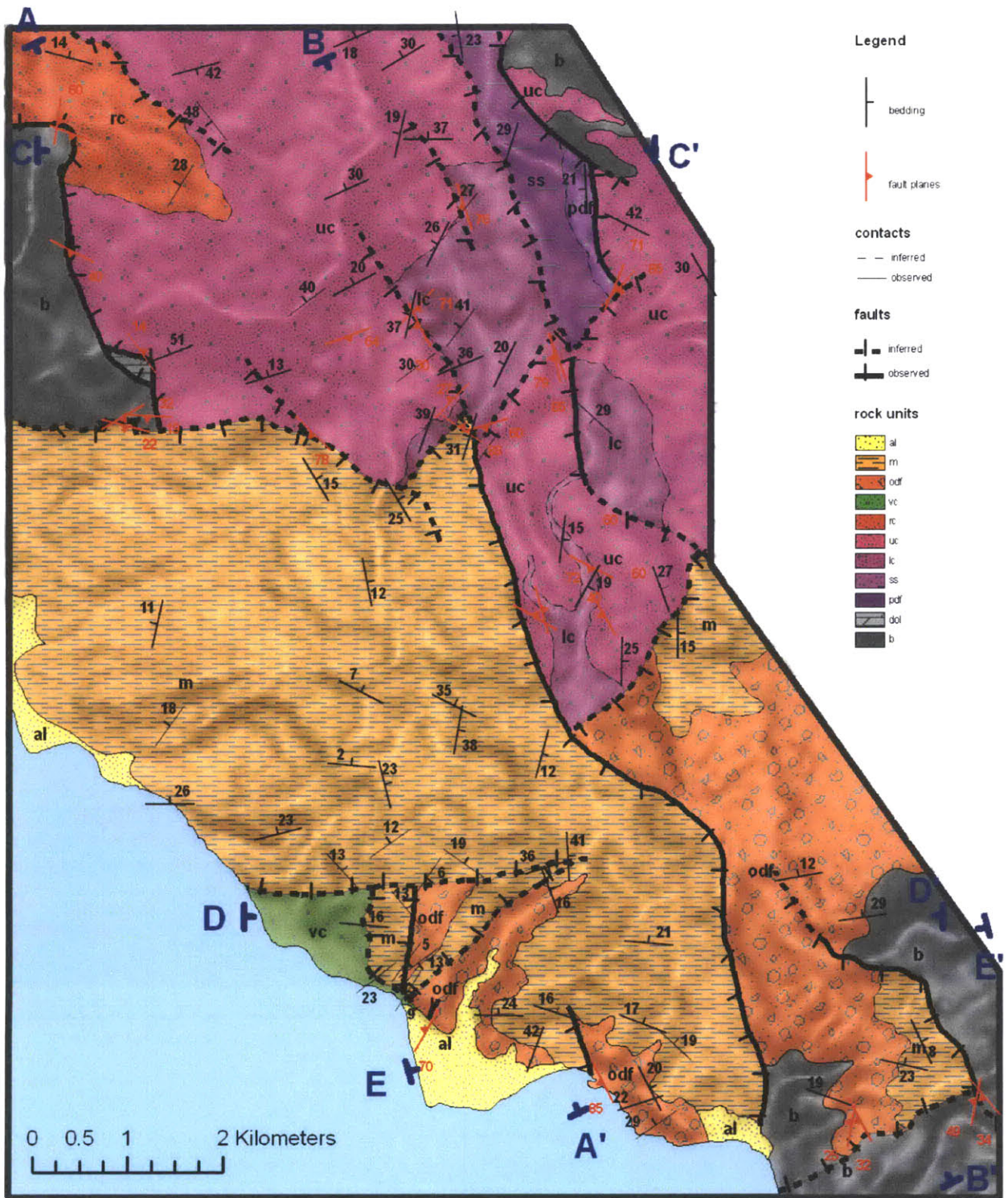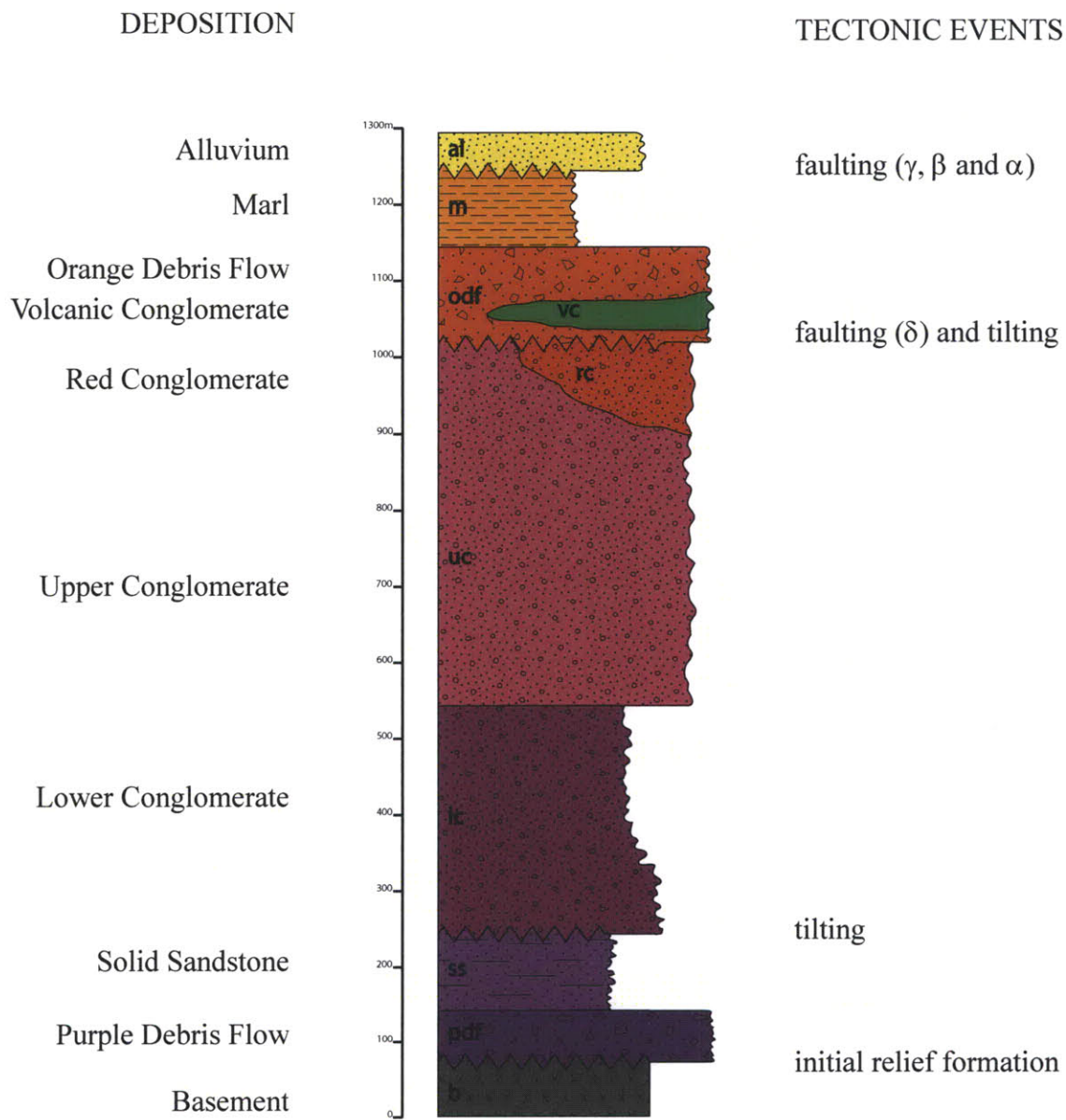
**Figure 3-2.** Stratigraphic column

42
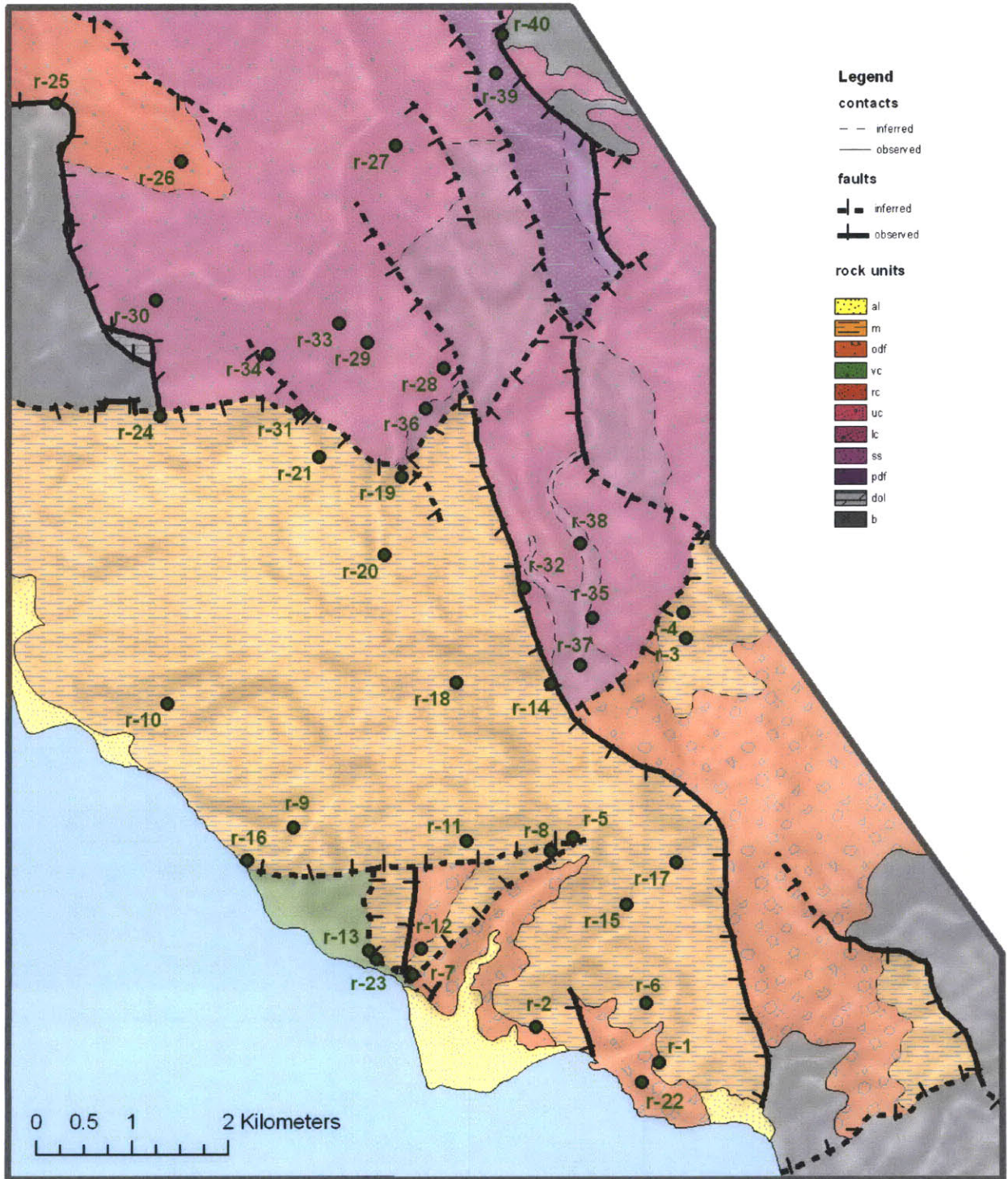
**Figure 3-3.** Lithology localities map

**Figure 3-4.** Conformable contact between Marl and Orange Debris Flow



**Figure 3-5.** Massive Marl outcrop
This outcrop of ~20 m thick marl is found along the road near the town of Limni, at locality r-1.

**Figure 3-6.** Siliciclastics within the Marl unit
The massive marl layer at r-1 is succeeded upward by grey and brown medium -
grained sandstones and fine-grained conglomerates.
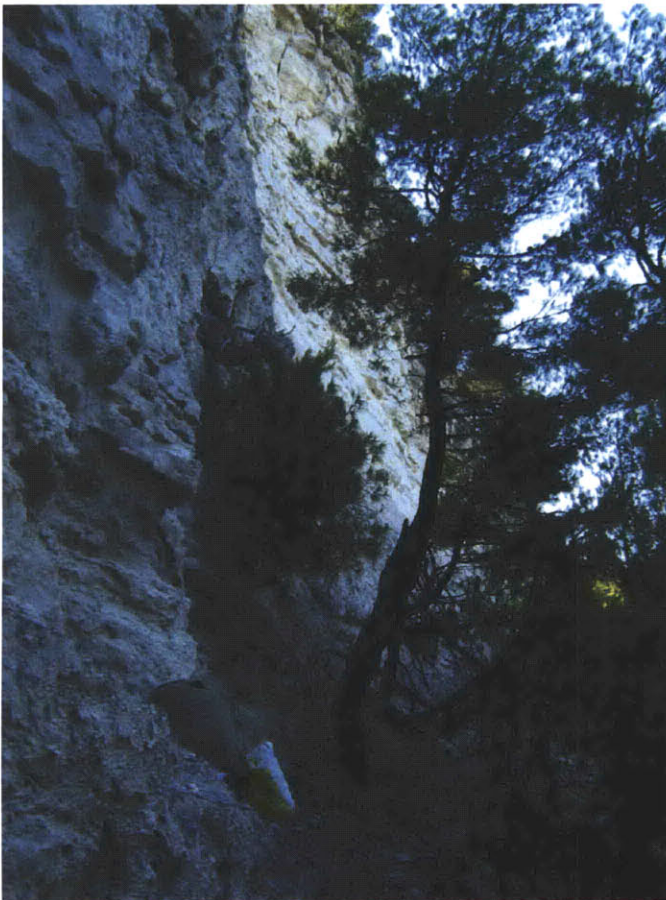


**Figure 3-7.** Limestone-rich marl cliff

**Figure 3-8.** Orange Debris Flow
Orange Debris Flow is semiconsolidated and clast supported with cm to dm scale well-rounded clasts. The clasts are mostly black and grey limestone (95%). Other clast lithologies include black and green gneisses, jasper and distinctive yellow rock with white veins. No clear stratification can be spotted.



**Figure 3-9.** Orange Debris Flow with sandstone interbeds
Orange Debris Flow (1) is estimated at ~100m thickness. At r-22 there is ~20 m of finer siliciclastics (2) suggesting a temporary decrease in the energy of the depositional flow.

**Figure 3-10.** Andesitic clast of the Volcanic Conglomerate
Hornblende, pyroxene, amphibole and quartz are the main minerals in these clasts.



**Figure 3-11.** Volcanic Conglomerate
At locality r-23 conglomerate with volcanic clasts (1) unconformably overlies a
debris flow equivalent to the Orange Debris Flow unit (2).

**Figure 3-12.** Red Conglomerate
This unit is characteristically a bright red color. The clasts are mostly limestone.
Bedding is clear and shallowly dipping.



**Figure 3-13.** Upper Conglomerate
Upper Conglomerate is well silicified, very hard and is a cliff former.

**Figure 3-14.** Upper Conglomerate supporting high topography
The highest mountain (927m) in the field area is built of Upper Conglomerate.



**Figure 3-15.** Red alteration in Upper Conglomerate

**Figure 3-16.** Interbed of finer material in Upper Conglomerate
Around the midpoint of Upper Conglomerate there is a distinctive fine-grained succession several meters thick that includes limestones, sandstones and mudstones. Cross-stratification features indicate that the unit of not overturned.



**Figure 3-17.** Cross-stratification in Upper Conglomerate
Pencil shows direction upsection. The unit is not overturned.

**Figure 3-18.** Lower Conglomerate
Lower Conglomerate is similar to the Upper Conglomerate, but it is less silicified and has higher sandstone content. Lower Conglomerate beds are generally matrix supported with well-sorted clasts and sandy matrix. Frequent sandstone interbeds demonstrate a clear stratification.



**Figure 3-19.** Red alteration in Lower Conglomerate
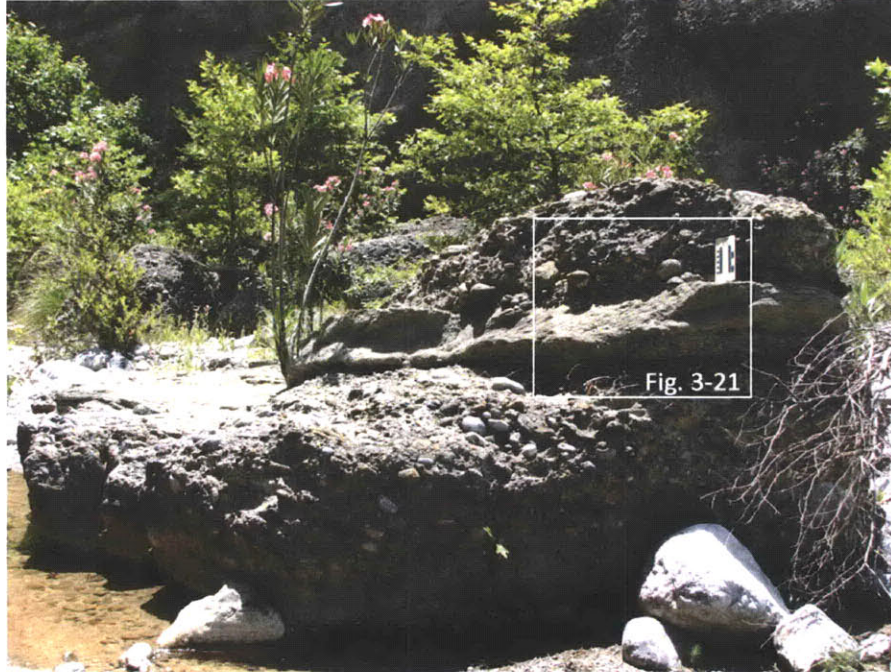
**Figure 3-20.** Cross-stratification in Lower Conglomerate
This well preserved sandstone bed at locality r-35 exhibits clear sedimentary structures.
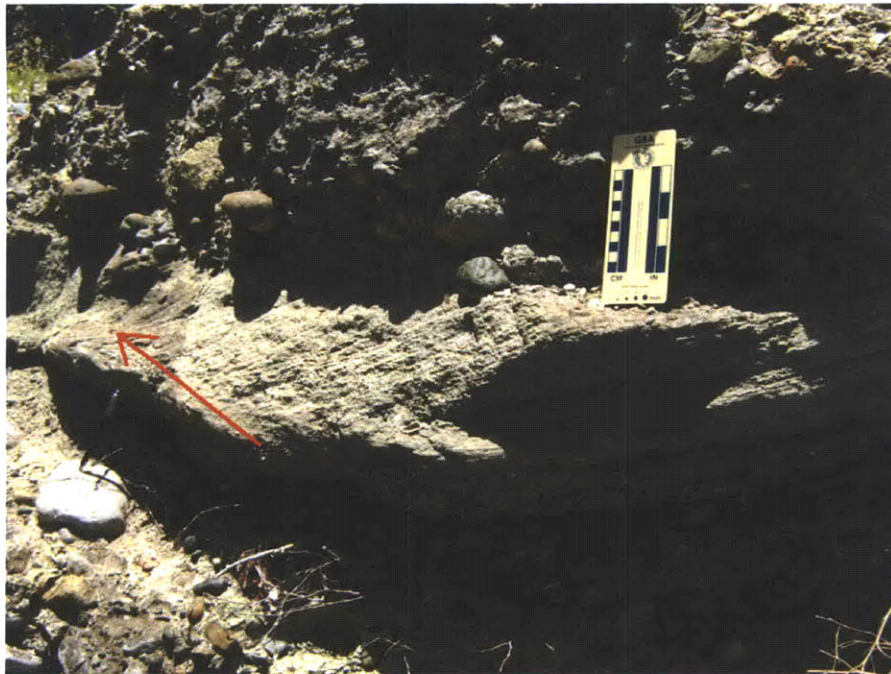


**Figure 3-21.** Cross-stratification in Lower Conglomerate
The cross-stratification is an evidence of the paleoflow direction (red arrow) to the south.

**Figure 3-22.** Conformable contact between Upper and Lower Conglomerate
At r-3 transitional contact from Lower Conglomerate to Upper Conglomerate
can be observed.



**Figure 3-23.** Solid Sandstone
Solid Sandstone is characterized by a high degree of cementation and by fine grain
size. It is very well stratified with well-sorted sandstone beds several cm thick and
frequent mudstone interbeds.

**Figure 3-24.** Purple Debris Flow



**Figure 3-25.** Purple Debris Flow clasts
The clasts are mostly green metamorphic or igneous rocks. Purple Debris Flow
is clast-supported with a characteristic purple siliceous matrix.
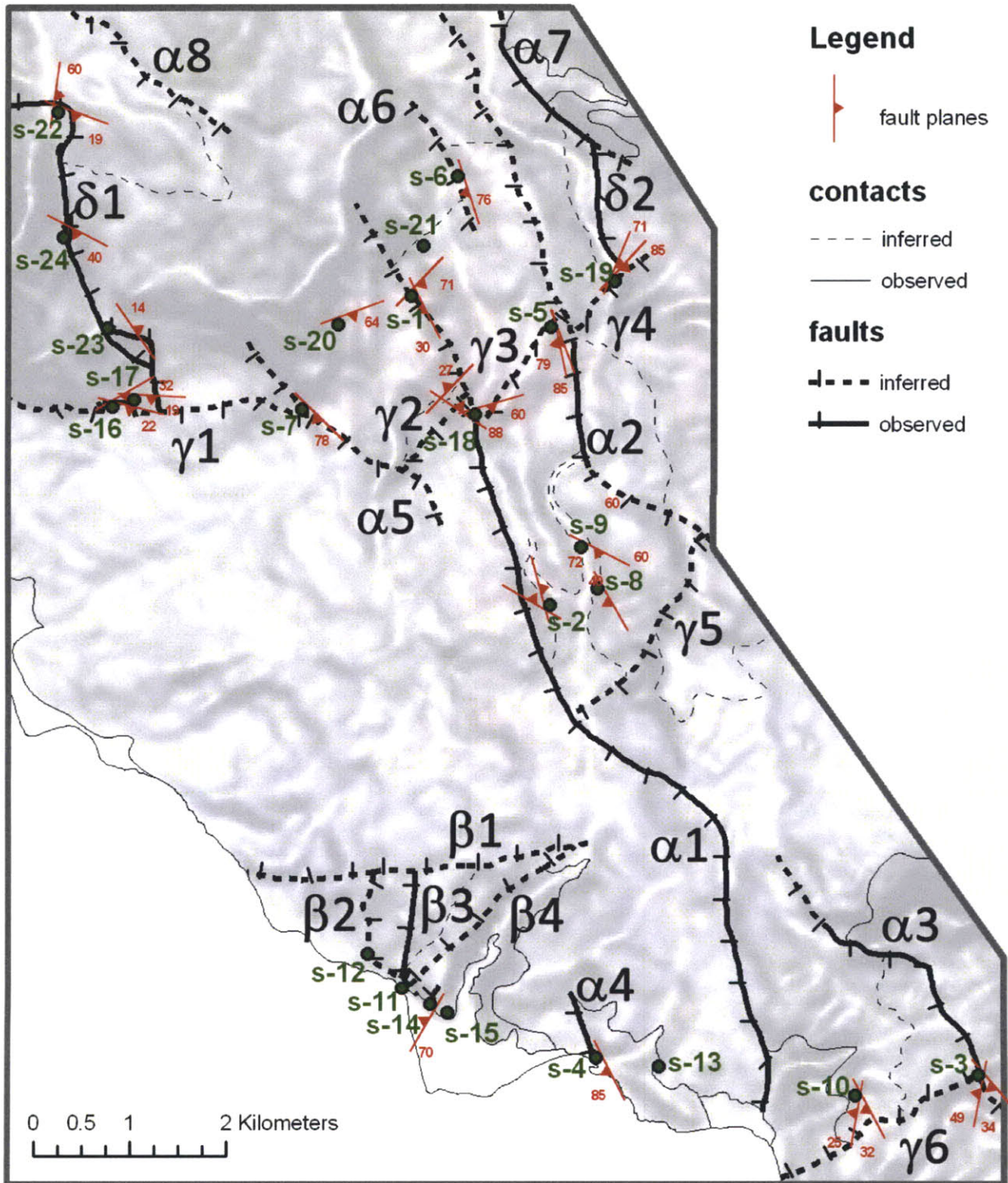
**Figure 4-1.** Structure map
Faults are labeled with Greek letters and numbers as in the text. Green points are the localities as discussed in the text.
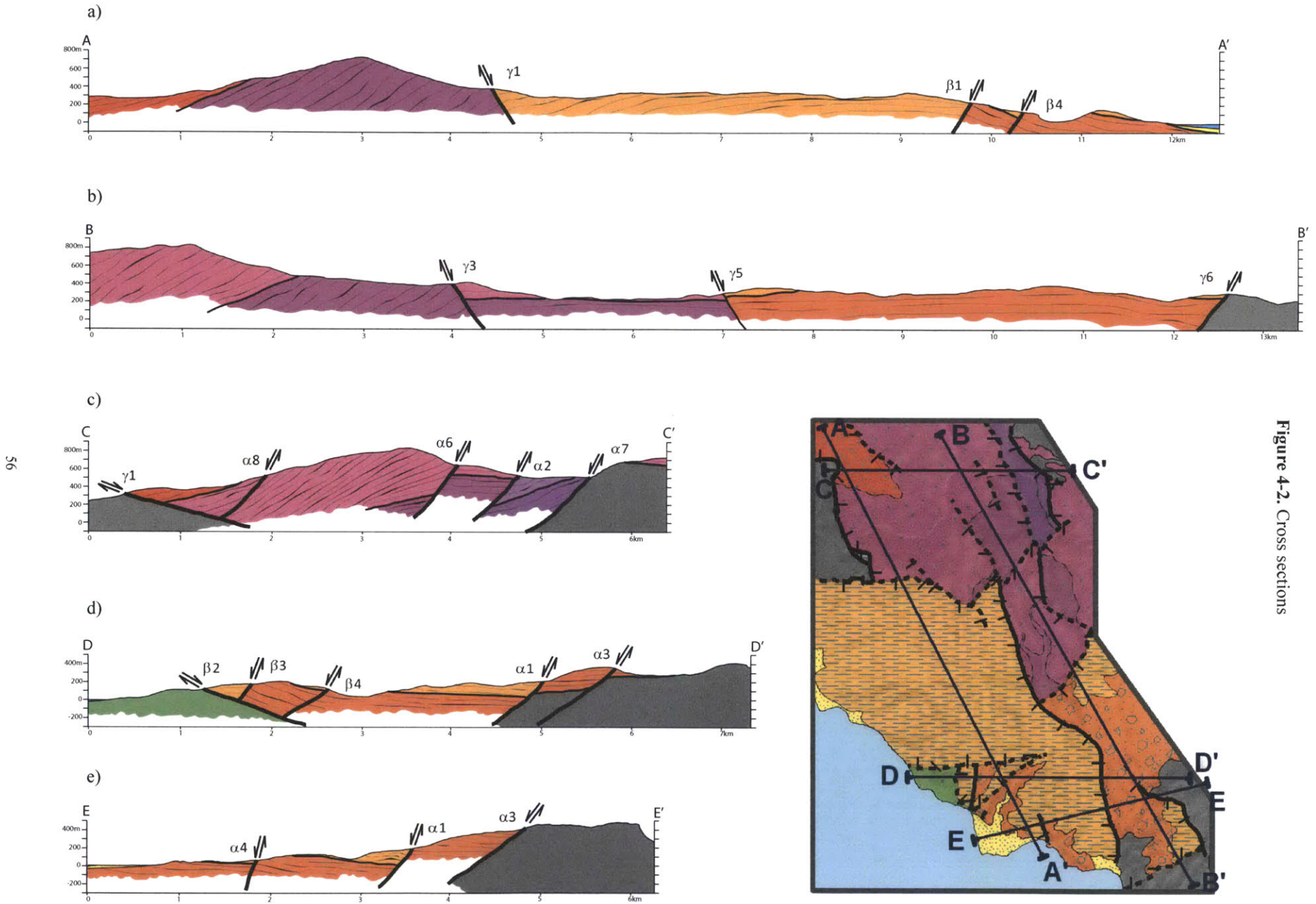
**Figure 4-2.** Cross sections

**Figure 4-3.** Minor normal fault within Lower Conglomerate



**Figure 4-4.** Strike-slip fault α4
Fault plane with NW-SE trending slickenlines separates Marl (1) and Orange Debris Flow (2).

**Figure 4-5.** Normal fault α5 within Upper Conglomerate
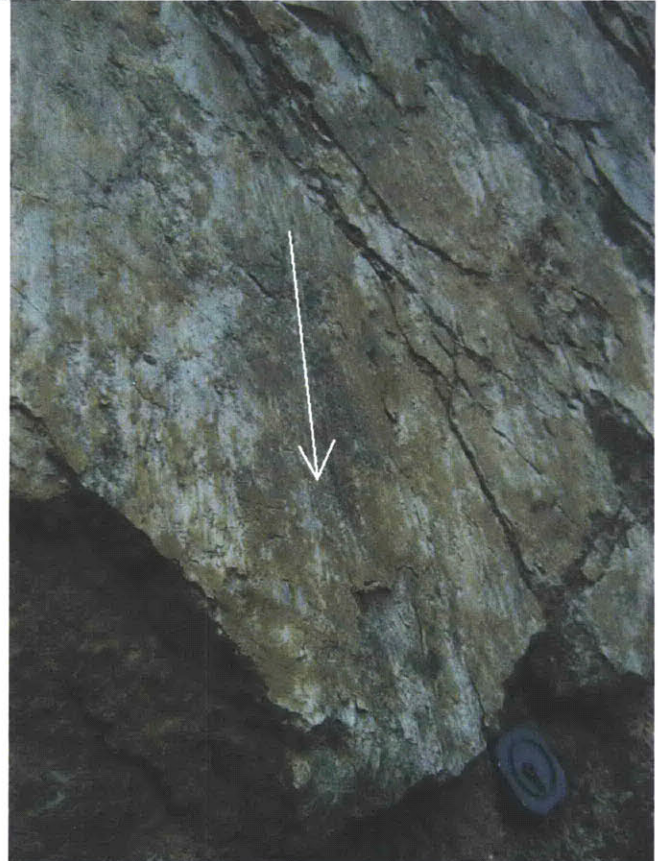


**Figure 4-6.** Slickenlines on fault α5 surface

**Figure 4-7.** Set of faults associated with set α



**Figure 4-8.** Faults at locality s-11
Low angle fault β2 (bottom) separates the Volcanic Conglomerate (3) and the Marl (1) and Orange Debris Flow (2 and 4). Fault β3 (left) is higher angle and separates Marl from the conglomerate. The fault on the right is within the Orange Debris Flow unit.

**Figure 4-9.** Detachment fault β2
Fault β2 separates Marl (1) and Volcanic Conglomerate (2).



**Figure 4-10.** Shallow fault γ1
Fault γ1 separates basement gneiss (1) and basin deposits (2).

**Figure 4-11.** Fault γ4 surface



**Figure 4-12.** Slickenlines on fault γ4 surface

**Figure 4-13.** Low angle fault δ1
The shallow tectonic contact separates the basement gneiss (2) from basin's Red
Conglomerate (1).



**Figure 4-14.** Mullions on fault δ1 surface

**Figure 4-15.** Carbonate lens on fault δ1
Shallow tectonic contact separates basement units (2) form the brecciated
carbonate (1).



**Figure 4-16.** Minor normal offsets in the basement
The contact between brecciated carbonates (2) and basement redbeds (1) is cut by
minor normal faults.

**Figure 4-17.** Folds within basement units
Isoclinal folds overturned to the northwest are preserved in the basement redbeds.



**Figure 4-18.** Fold within basement units
Bigger scale fold in basement's gneiss.
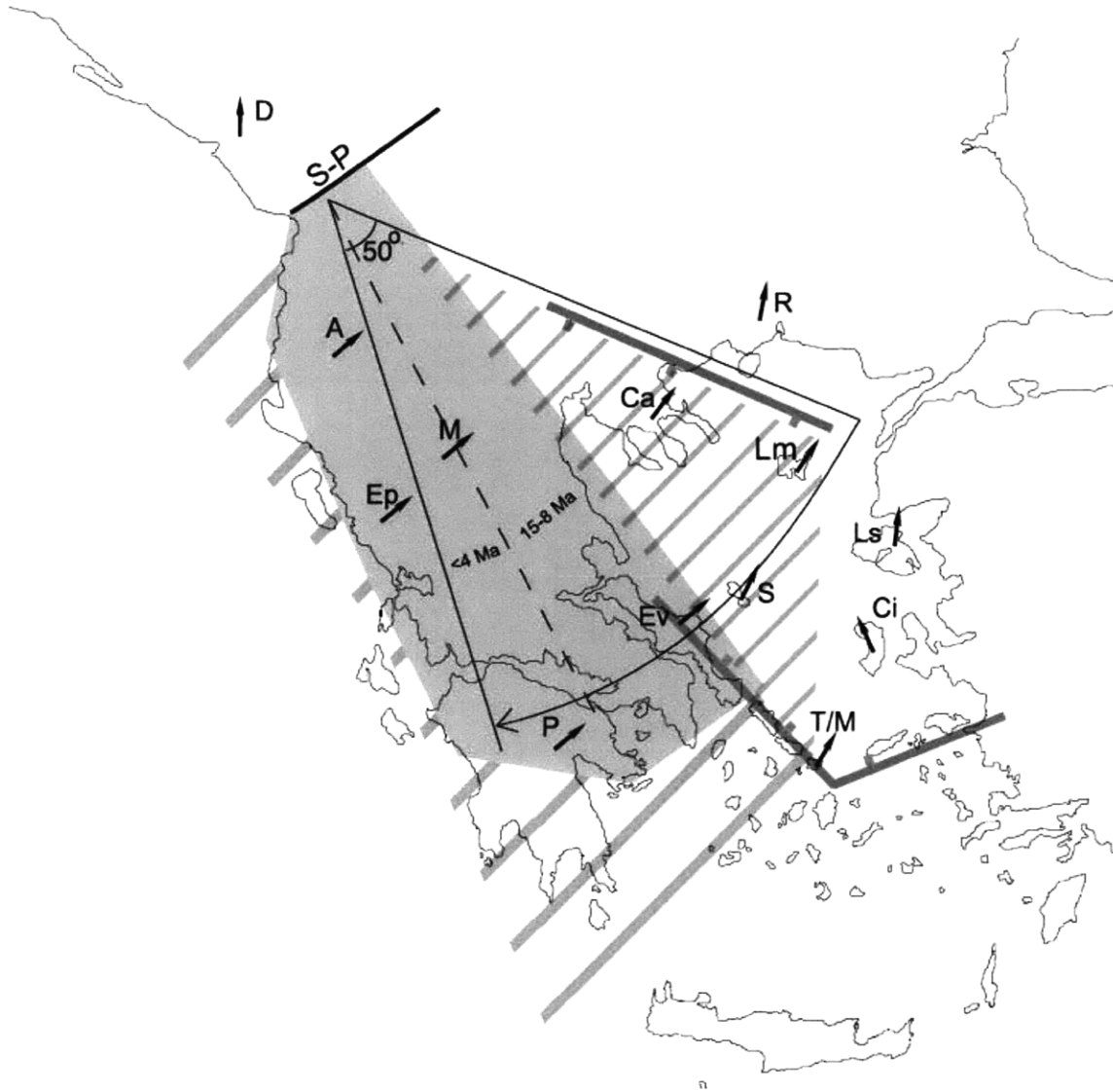
**Figure 5-1.** Rotation in the Aegean since the Miocene
(from van Hinsbergen et al., 2005)
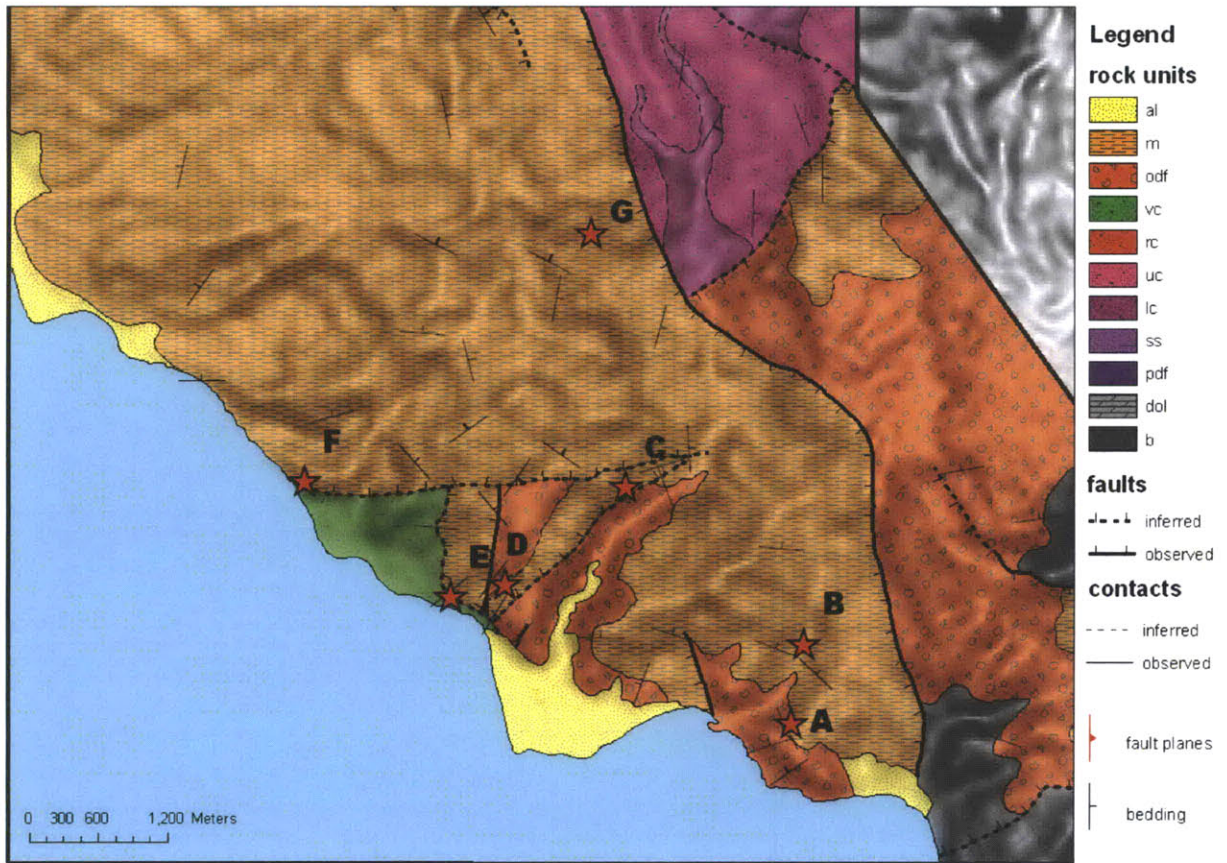
**Figure 5-2.** Paleomagnetic sampling localities
Samples were drilled in seven localities (A through G) in southern part of the field area, within the Marl unit.
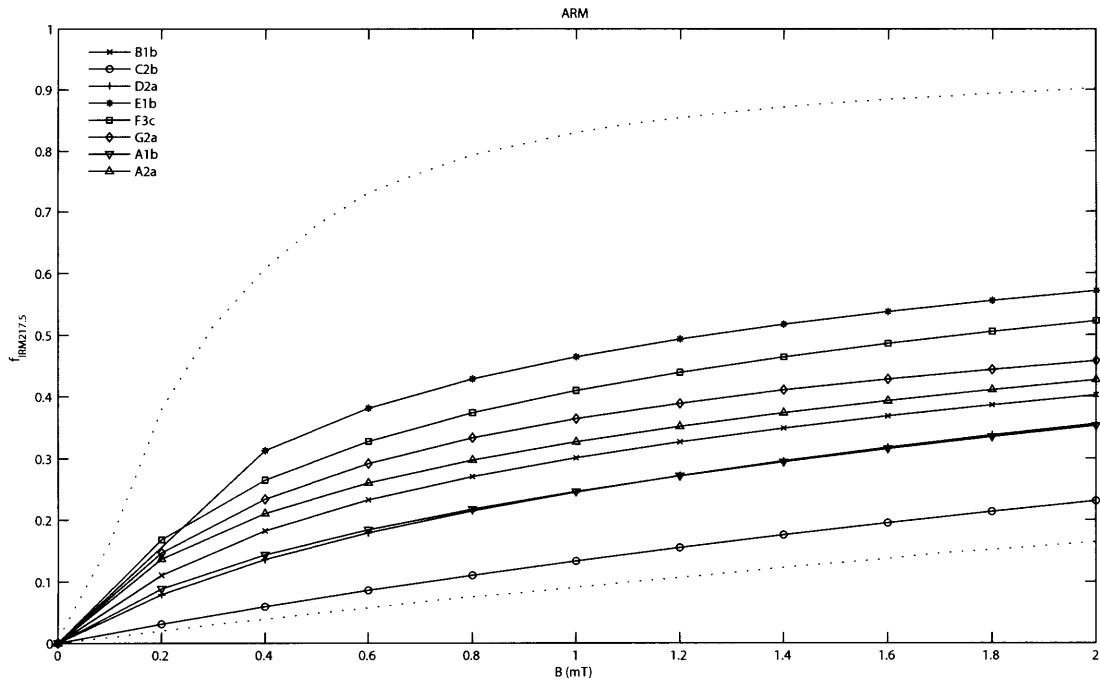
**Figure 5-3.** ARM

ARM acquisition as a function of DC bias field. The lower dashed line represents a sample where grains interact strongly with each other (SD), the upper line represents non-interacting samples. Samples in this study are strongly interacting.
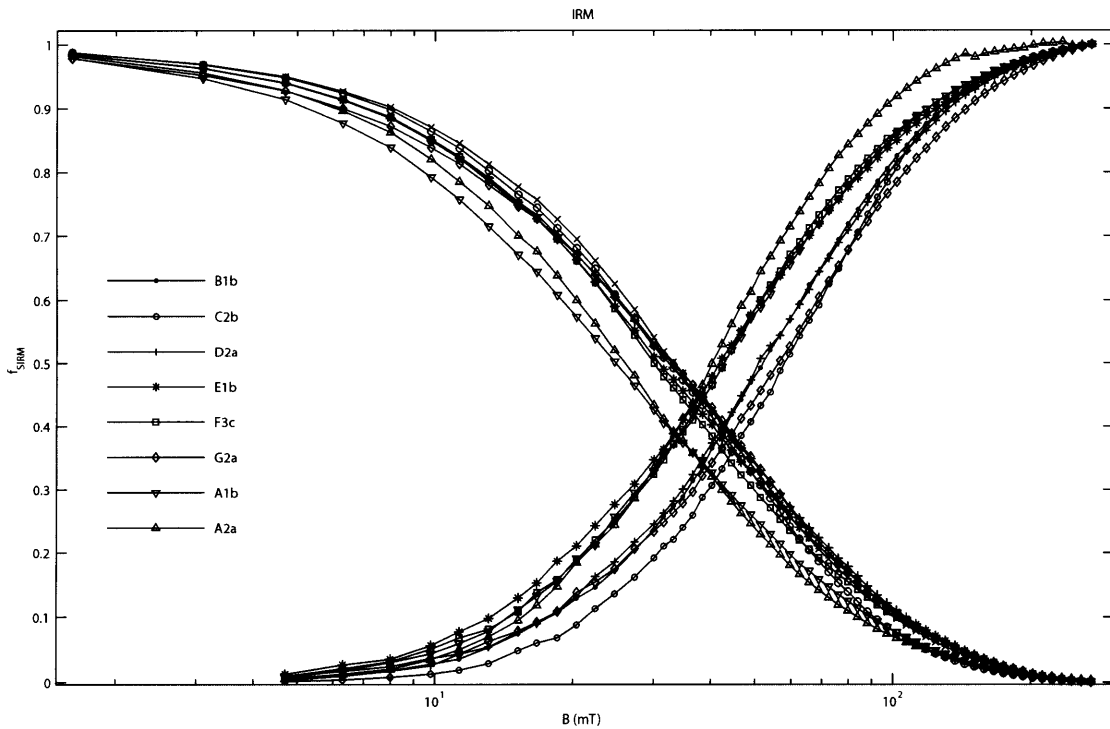


**Figure 5-4.** IRM

IRM acquisition (increasing) versus progressive demagnetization of IRM with alternating fields (decreasing) is plotted as a function of the applied field (AF). Only sample A2 is saturated by 300mT. All of the cross-over points (R) are below 0.5, indicating a strong interaction between the grains.
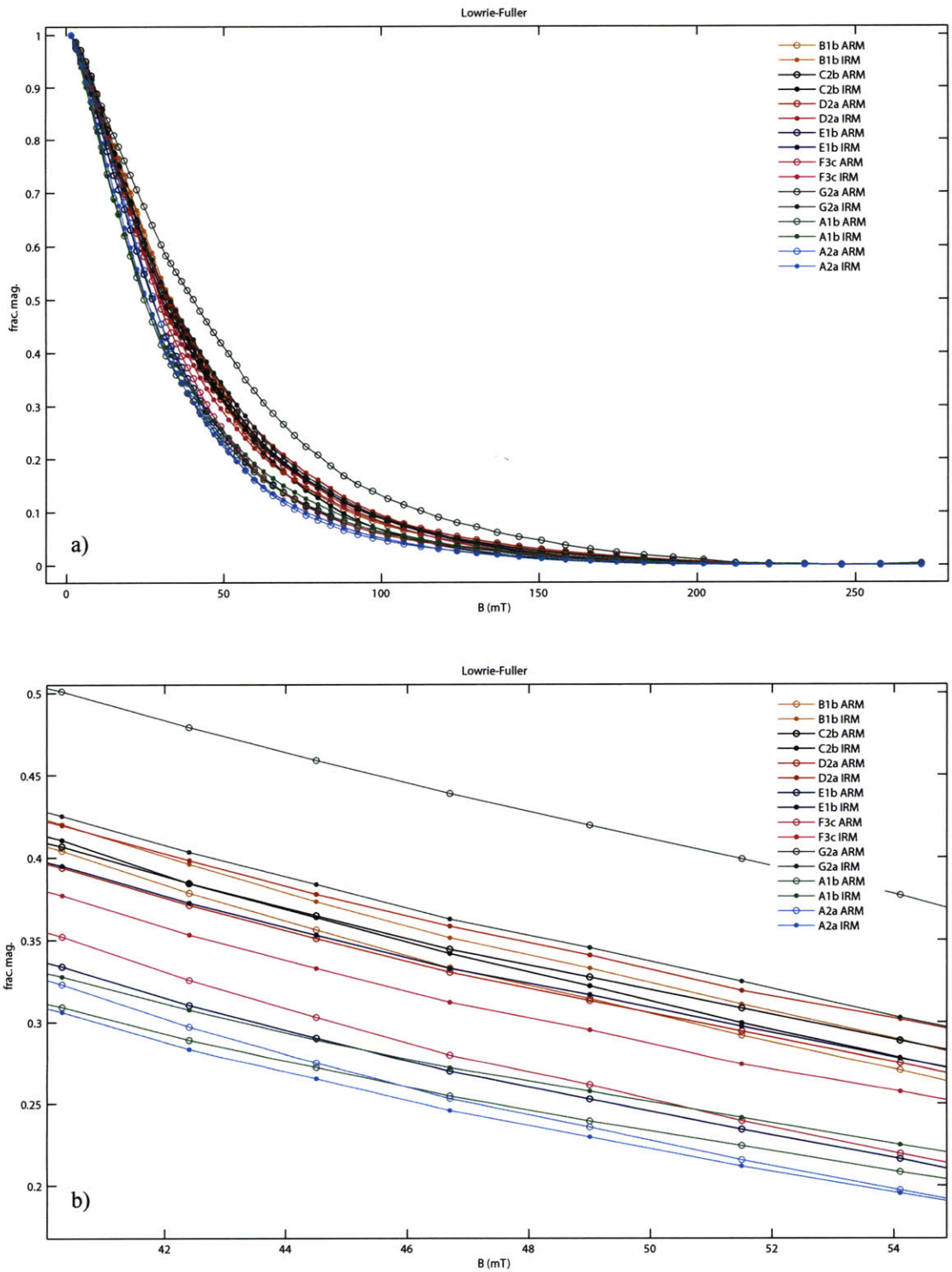
**Figure 5-5.** Lowrie-Fuller test
The Lowrie-Fuller test compares the ARM and IRM demagnetization curves for various
applied fields. The curves lie very close to each other (a), making the interpretation inconclusive.
Zoomed-in picture (b) reveals that for most of the samples ARM is smaller than IRM, only for
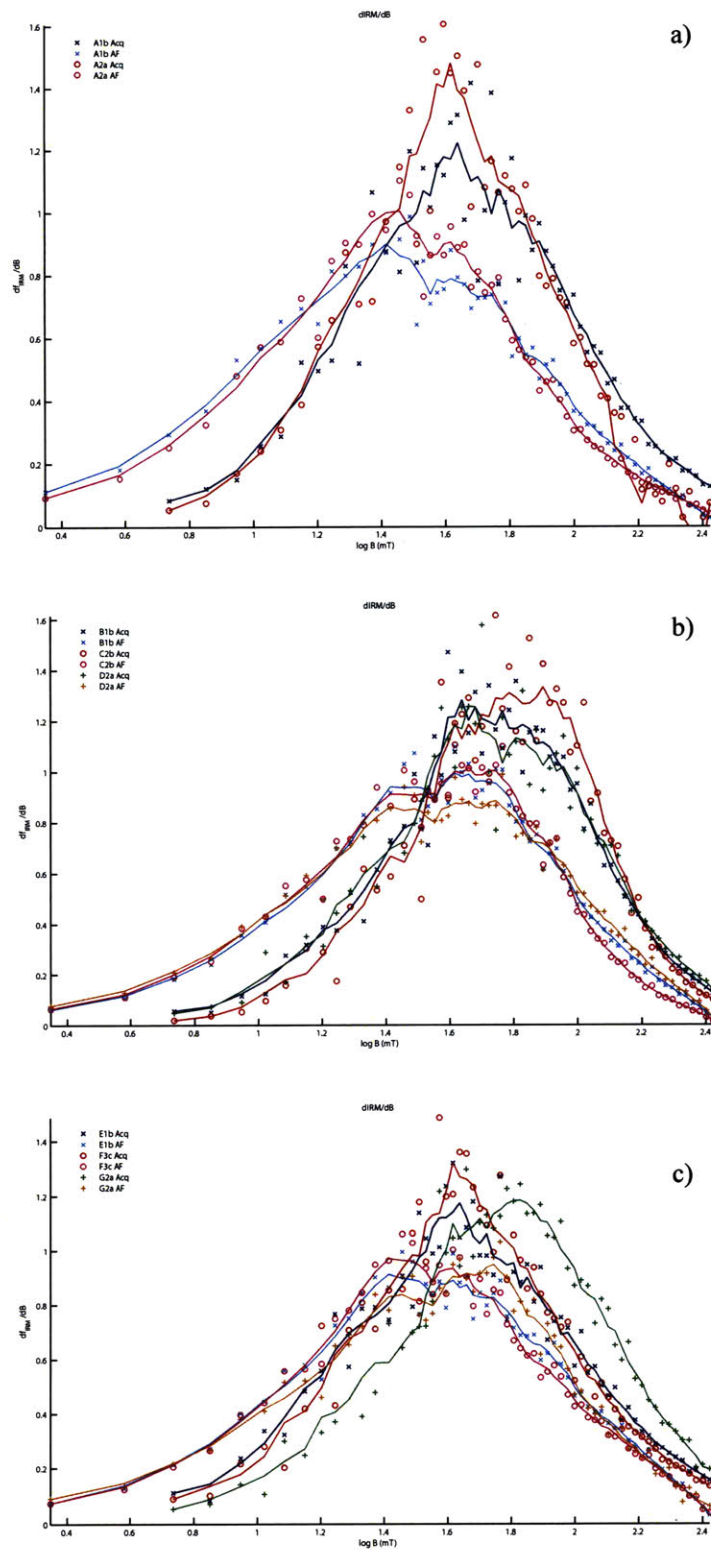C2 and G2 ARM is greater than IRM.

**Figure 5-6.** IRM derivative
Derivative of the IRM demagnetization (AF) and acquisition (Acq) curves were derived for samples A1 and A2 (a), B1, C2 and D2 (b) and E1, F3 and G2 (c). It is clear that all of the samples exhibit bimodal distribution, which is more clearly pronounced in the AF curves. The samples have a complicated magnetic coercivity spectrum and include more than one type of magnetic mineral.
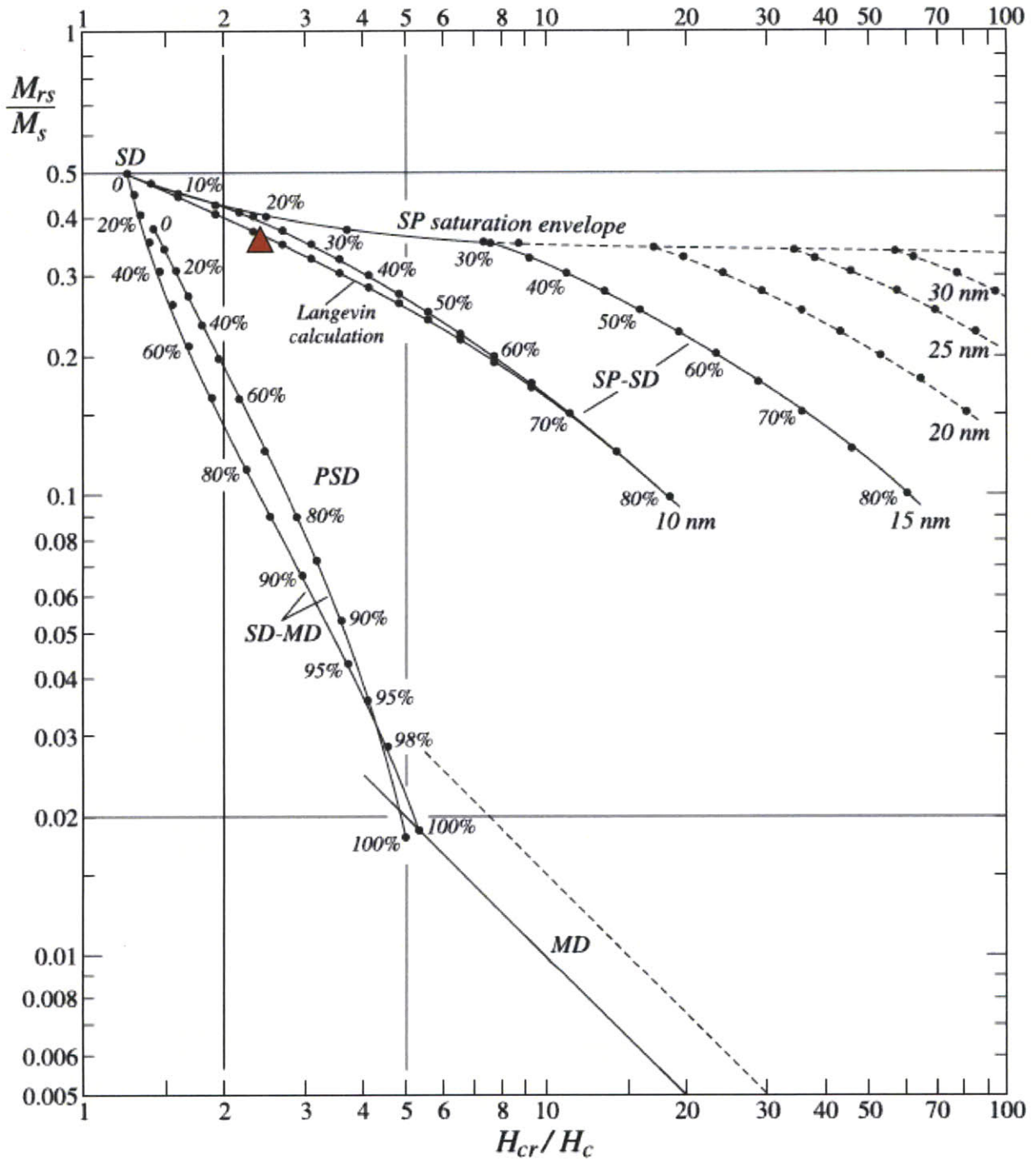
# Theoretical Day plot curves for magnetite



**Figure 5-7.** Day plot
The samples from this study (red triangle) fall into the pseudo-single domain group.
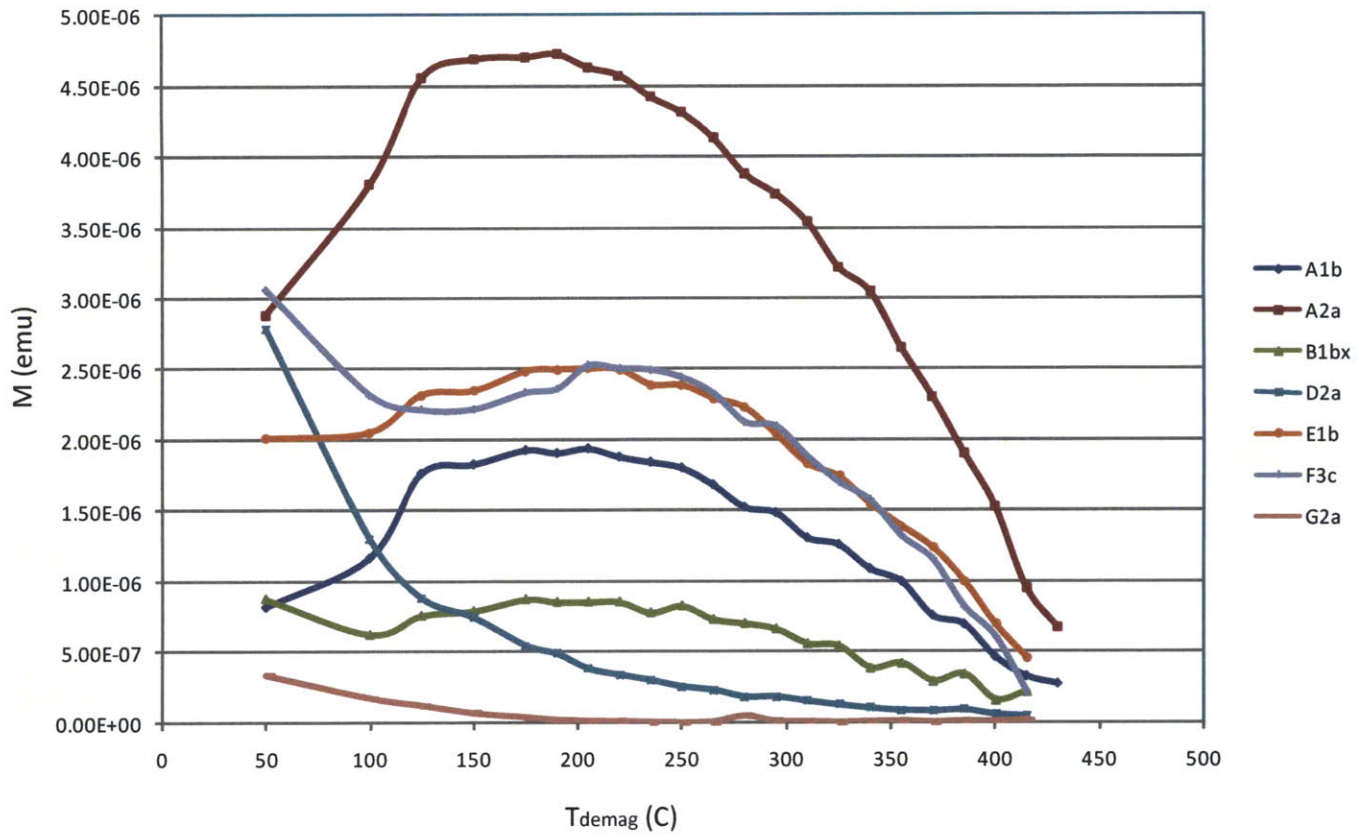(adapted from Dunlop, 2002a)

**Figure 5-8.** Magnetic moment decay
The magnetic moment (M) of the samples started at a low level and decayed quickly with the demagnetization temperature increase. By the time the samples were heated up to 430C, M was so small that the errors were relatively too large to obtain meaningful results and the experiment was stopped.
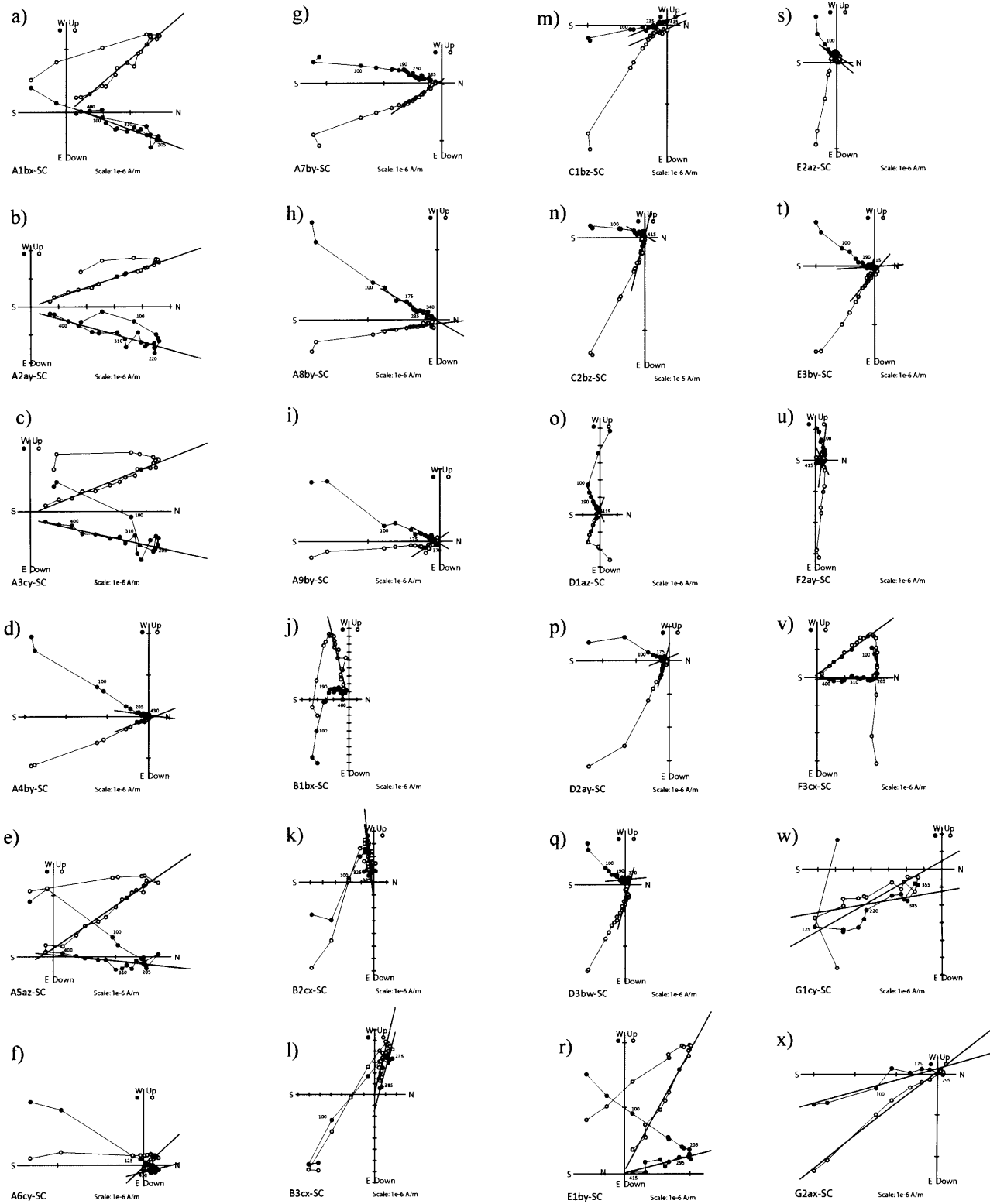
**Figure 5-9.** Zijderveld diagrams of the analyzed samples

Samples from all sites are plotted in core coordinates with the best fit line for the HT component. Samples A and B (a to l) show a clear current field overprint and primary component. Samples C and D (m to q) get demagnetized quickly, but they still yield good HT directions. Samples E1 and F3 (r and v) give good HT directions. The rest of the samples (localities E and F) are quickly demagnetized. No sensible result for G (w and x).
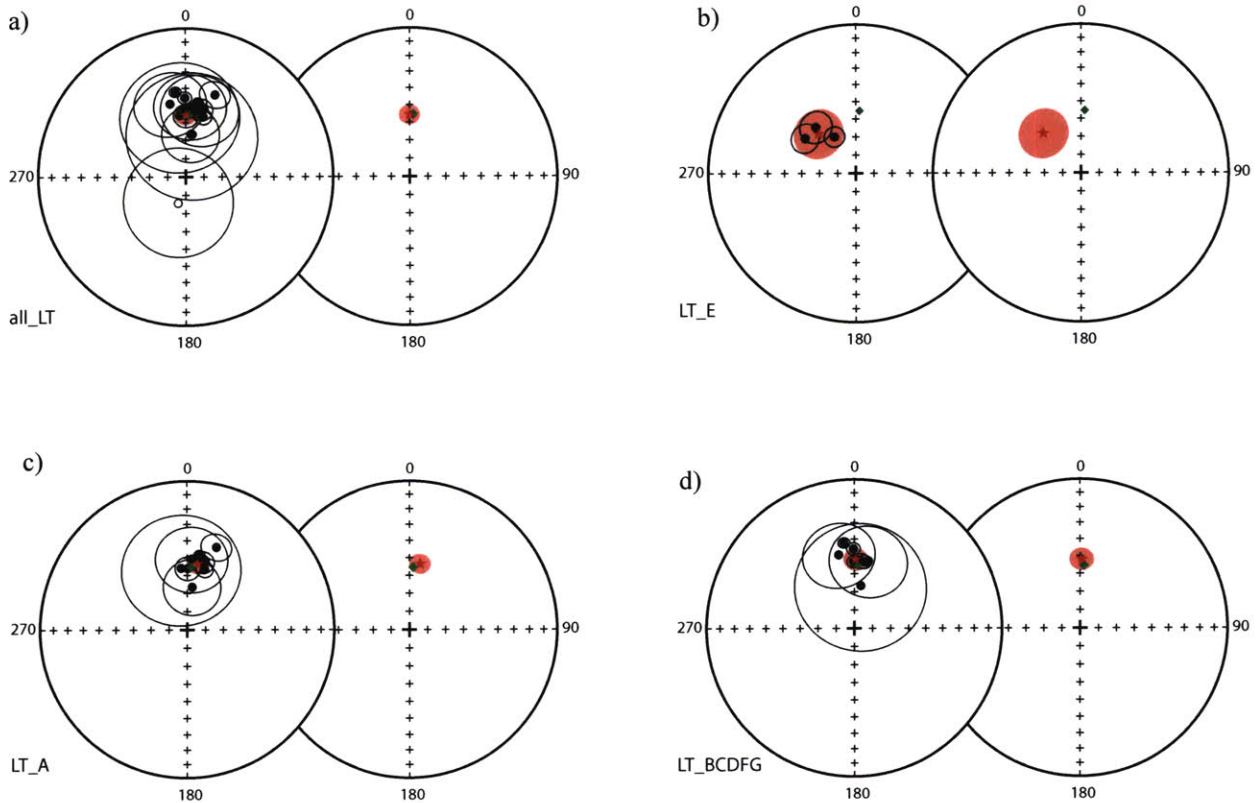
72

**Figure 5-10.** Current magnetic field overprint
The plots are based on the data in Table 3. Red stars are the means for given sets of data; the means are also plotted in a separate stereonet for clarity. Green diamond is the current magnetic field in Greece.
It is clear that the mean for all the data in the basin (a) is consistent with the current field direction. Only at locality E (b) the lower temerature (LT) component is not consistent with the current field.
In c) and d) the data are plotted separately for locality A (c) and for localities B, C, D, F and G (d) to show that there is no inconsistency in terms of the LT as it is the case with the HT component (Figure 5-11).
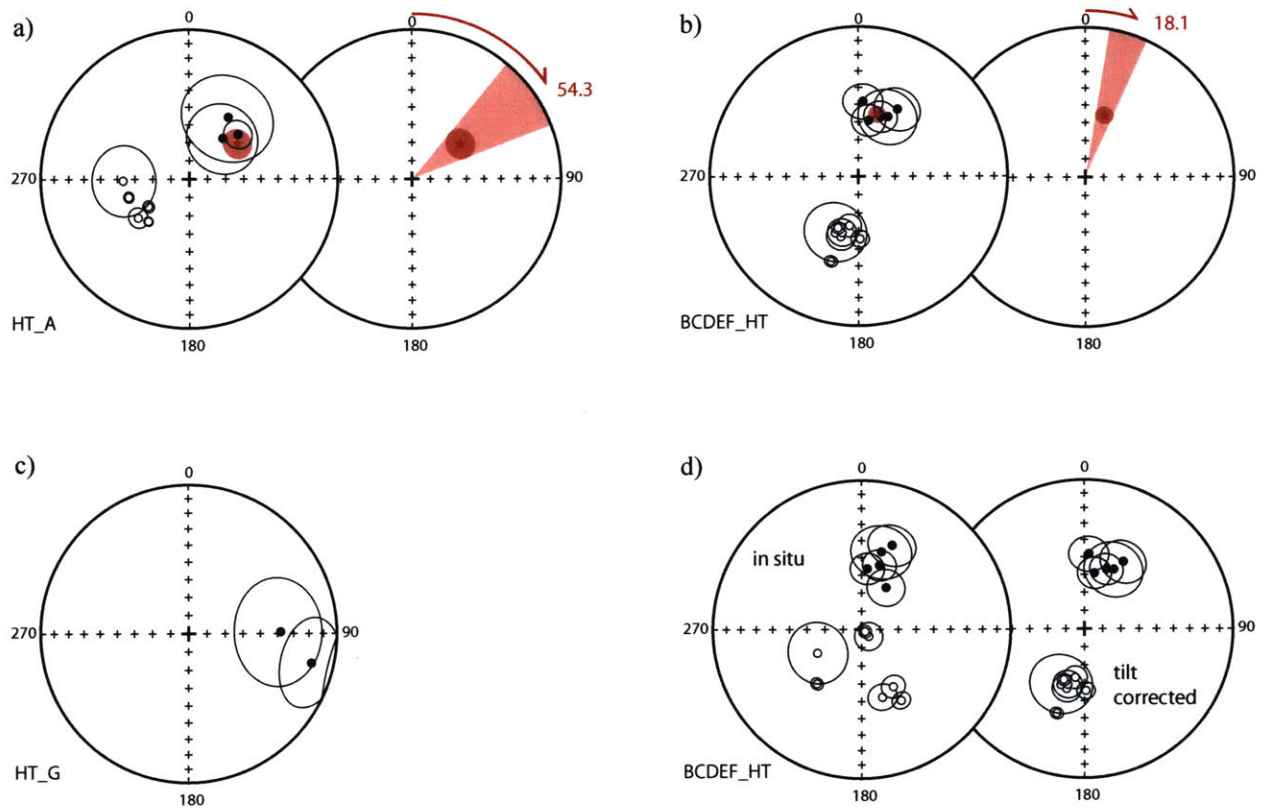
**Figure 5-11.** Primary magnetization direction
Data from locality A yield 54.3 degrees of clockwise rotation (a). For the rest of the localites the data is very consistent and significantly smaller than A. The representative rotation for the basin is 18.1 degrees clockwise and comes form localities BCDEF (b). Locality G is inconsistent with the rest of the data (c) and was excluded form the rotation analysis. The limestones at locality G must have been altered after the deposition so that the primary magnetization direction was obscured. Data from BCDEF passes the fold test. On (d) it is clear, that the data points are more alligned after applying the tilt correction.
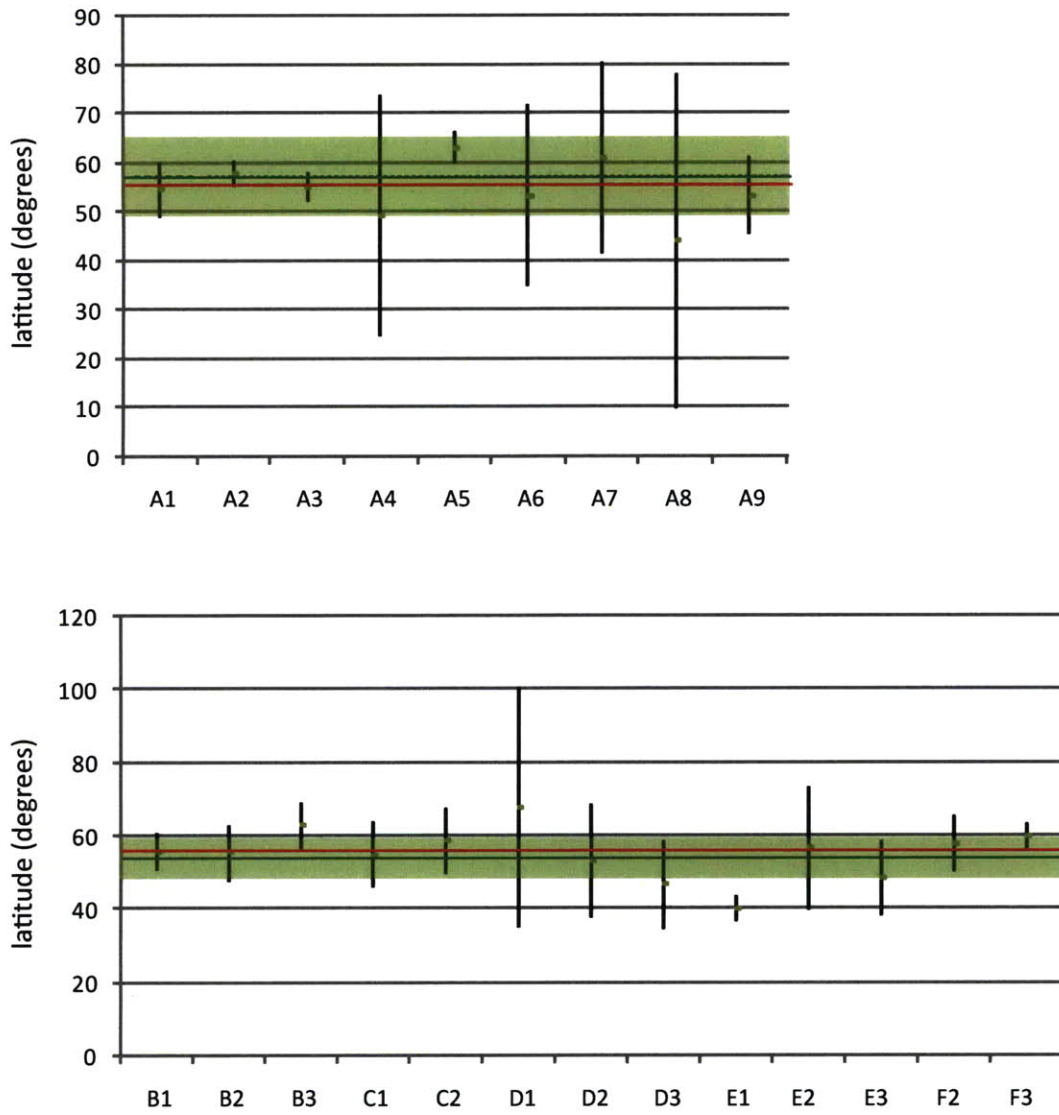
**Figure 5-12.** Paleolatitude
For both localities, A and BCDEF, current latitude of Greece (red) falls within the error of the mean of the paleolatitudes derived from the HT component directions (green).